

**Master Thesis**

**Dark Halo:**

**Enigmatic Features of Dark Streaks  
at Martian Volcanoes**

**Takenori Toyota**

**Earth and Planetary System Science Group  
Department of Earth & Planetary Science  
Graduate School of Science, The University of Tokyo**

**January 26, 2009**

## Abstract

On the planets having atmosphere such as Mars, there are various types of interactions between the atmosphere and the ground surface. Such interactions cause observable changes in the surface patterns. Polar caps and aeolian features are typical examples. With the accumulation of satellite-based exploratory data, time-variable surface patterns have been recognized and investigated extensively, because they can be direct indicators of the changing surface environments. Here we report a new kind of time-variable surface pattern called “Dark Halo” near the top of high altitude volcanoes in Tharsis region. Recent continual and high-resolution observations have revealed enigmatic features of “Dark Halo”:

1. “Dark Halo” is composed of assemblage of dark spire-shaped streaks, hereafter we call “Spire Streaks”.
2. Each streak starts from a point-like very narrow region.
3. In most cases, no topographical obstacle can be identified at the initiation point.
4. Each “Spire Streak” starts at high position and increases its width downward.
5. “Dark Halo” and “Spire Streak” universally exist near the top of high mountains (Olympus, Elysium, Pavonis and Ascraeus) although the actual heights are not uniform.
6. “Dark Halo” shows temporal changes in its pattern.

These features are not compatible with existing models of aeolian streaks.

Data from visible imagers, imaging spectrometers, a laser altimeter and a numerical modeling are investigated to understand the formation process of “Spire Streak” and “Dark Halo”.

As a result of such investigations, the author proposes two possible origins of “Spire Streaks” and “Dark Halo”: 1) erosion of fine dust by gusty strong slope wind, and 2) deposition of wind-blown volatiles. Both origins are completely new kind of wind-surface interactions that haven't ever discovered.

Future work will contain analysis of spectral data that are produced by recent high-resolution instruments to know the difference between surface materials on “Dark Halo” and on its surrounding region.

## 要旨

火星のように大気をもつ惑星では、大気と地面の間に様々な相互作用がある。そのような相互作用の結果として、観測可能な変化が惑星表面に生じる。火星における代表的な例が風成痕 (Wind Streak) や極冠の氷などである。周回軌道からの長期観測によって、表面の様子が時間変化することがわかった。こういった変化は表層環境を知るための重要な手掛りと考えられており、多くの科学者が研究の対象としている。

本研究の目的は、火星表面の時間変化する模様の一つである「Dark Halo」の成因を明らかにすることにある。最近の継続的かつ高解像度の観測によって、これまでの理論では説明できない「Dark Halo」の特徴が明らかになってきた。すなわち、

1. 尖塔形をした「Spire Streak」という構造の集合体が「Dark Halo」を形成している。
2. 「Spire Streak」の先端は尖っており、ほぼ点に近い。
3. ほとんどの場合、「Spire Streak」の先端部には特別な地形や障害物が無い。
4. 「Spire Streak」の尖った部分は高度が高い側に存在し、高度が低い側にいくにつれて広がっている。
5. 火星の高度が高い火山では、「Dark Halo」と「Spire Streak」が共通して見られる。
6. 「Dark Halo」の形は時間変化する。

ということである。このような特徴は既存の理論では説明がつかない。

「Dark Halo」の形成過程が明らかになれば、表面に残された模様から表層環境に関する定量的なデータが得られるようになる。すなわち、着陸機が存在しない場所の表面情報を推定する方法として、画像解析が有効になるのである。

著者は「Dark Halo」の形成過程を明らかにするため、NASA 及び ESA の探査機が取得した可視・赤外の画像を解析した。その際、レーザー高度計による地形モデルや数値気候モデルとの比較も行った。

その結果、著者は「Spire Streak」と「Dark Halo」の形成過程として2つの可能性を導きだした。すなわち、

- 突発的な強い斜面風によって、表面の細かなダストが侵食される過程。
- 地下からの噴出物が拡散し、堆積する過程。

である。さらに2つの可能性から1つに絞るため、解像度の高い分光画像を解析し「Dark Halo」とその周辺部分の構成物質の違いを明かにするのが今後の課題である。

# Contents

|          |                                                                            |           |
|----------|----------------------------------------------------------------------------|-----------|
| <b>1</b> | <b>Introduction</b>                                                        | <b>1</b>  |
| 1.1      | General introduction to Mars . . . . .                                     | 1         |
| 1.1.1    | Past spacecraft missions . . . . .                                         | 1         |
| 1.1.2    | Surface environment . . . . .                                              | 2         |
| 1.1.3    | Volcanism on Tharsis . . . . .                                             | 12        |
| 1.2      | Introduction to this thesis . . . . .                                      | 13        |
| 1.2.1    | Cause for low albedo on Mars . . . . .                                     | 15        |
| 1.2.2    | Wind streaks on Mars . . . . .                                             | 17        |
| 1.2.3    | ”Dark Halo” at high altitude volcanoes . . . . .                           | 21        |
| 1.2.4    | Problems to be resolved in this thesis . . . . .                           | 22        |
| <b>2</b> | <b>Method</b>                                                              | <b>23</b> |
| 2.1      | Numerical modeling of surface pressure . . . . .                           | 23        |
| 2.2      | Laser Altimeter . . . . .                                                  | 23        |
| 2.3      | Visible imagers . . . . .                                                  | 24        |
| 2.4      | Imaging spectrometers . . . . .                                            | 28        |
| <b>3</b> | <b>Results</b>                                                             | <b>31</b> |
| 3.1      | Morphology and distributions . . . . .                                     | 31        |
| 3.2      | Temporal changes in patterns . . . . .                                     | 48        |
| <b>4</b> | <b>Discussion</b>                                                          | <b>52</b> |
| 4.1      | Possible origins of the spire streak derived from the morphology . . . . . | 52        |
| 4.2      | Material that cause temporal changes in patterns . . . . .                 | 54        |
| 4.3      | Possibility of the phase change phenomena at the dark halo . . . . .       | 54        |
| 4.4      | Cause for albedo difference . . . . .                                      | 62        |
| <b>5</b> | <b>Conclusion</b>                                                          | <b>64</b> |
| <b>6</b> | <b>Summary and Future Work</b>                                             | <b>65</b> |
|          | <b>Acknowledgements</b>                                                    | <b>66</b> |
|          | <b>References</b>                                                          | <b>67</b> |

# 1 Introduction

## 1.1 General introduction to Mars

Mars (Figure 1) is the fourth planet from the Sun in the Solar System. It is also referred as the "Red Planet" because of its reddish appearance. This reddish appearance is due to iron oxide. Mars is a terrestrial planet with a thin atmosphere, having surface features reminiscent both of the impact craters of the Moon and the volcanoes, valleys, deserts and polar ice caps of the Earth. It is the site of Olympus Mons, the highest known mountain in the Solar System, and of Valles Marineris, the largest canyon. Furthermore, In addition to its geographical features, Mars' rotational period and seasonal cycles are likewise similar to those of Earth.

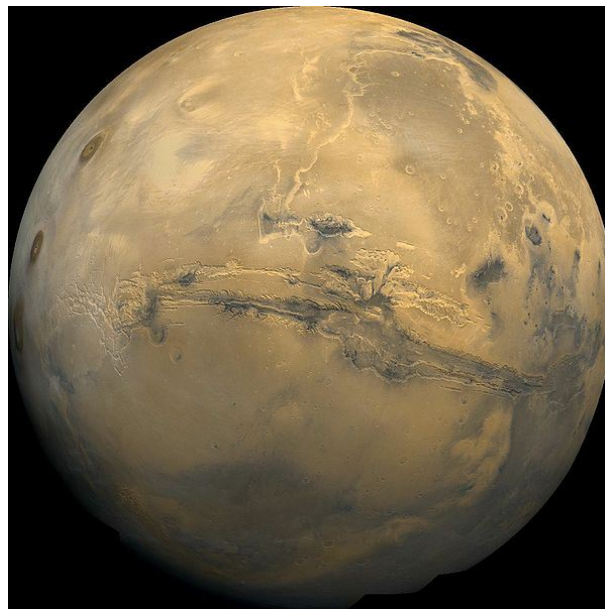


Figure 1: Mars (Image credit: NASA/JPL/Malin Space Science System).

### 1.1.1 Past spacecraft missions

Mars has been a major spacecraft destination ever since the early days of space exploration. A list of the missions that have been launched until 2007 and whose science data are now available is summarized in Figure 2. The United States began its spacecraft exploration of Mars in 1964 when it launched the Mariner 4 spacecraft. Mariner 4 became the first successful flyby mission to Mars. Mariner 4 confirmed that Mars is surrounded by an atmosphere primarily composed of carbon dioxide and that this atmosphere exerted

a surface pressure in the range of 500 to 1000 Pa. The discovery of channels formed by a flowing liquid, most likely water, was one of the most exciting results from the Mariner 9 mission. NASA's next two missions, Vikings 1 and 2, included landers that tested the soil to explore evidence of micro-organism. The Viking landers measured temperature, pressure, and composition of the atmosphere. The Viking orbiters mapped the entire surface of Mars and acquired over 52000 images. Mars Global Surveyor (MGS) produced high-resolution images with Mars Orbiter Camera (MOC). MGS Mars Orbiter Laser Altimeter (MOLA) used laser pulses to determine topography and roughness of the surface. MGS Thermal Emission Spectrometer (TES) provided information about the thermal properties of the surface and atmosphere as well as surface composition. Mars Pathfinder, the first successful rover, set down in the outwash region of Ares Vallis. The Thermal Emission Imaging System (THEMIS) onboard Mars Odyssey observed Mars in both visible and infrared wavelengths. The two Mars Exploration Rover (MER) missions, named Spirit and Opportunity, investigated sites that might contain evidence of ancient water and the early Martian climate. Mars Reconnaissance Orbiter obtained more data than ever acquired by other spacecrafts. Phoenix landed on Mars successfully, and found solid water beneath the dust-covered layer. European Space Agency successfully sent Mars Express orbiter to Mars. Mars Express High Resolution Stereo Camera (HRSC) produced spectacular three-dimensional images of Martian surface.

### **1.1.2 Surface environment**

#### **Atmosphere**

The Mars atmosphere is thin and composed largely of carbon dioxide. The surface pressure ranges from 600 to 900 Pa, less than one-hundredth of the atmospheric pressure at sea level on Earth. The pressure varies with seasons as a part of atmosphere condenses on the winter pole (Figure 3). The pressure cycle is highly repeatable from year to year. The scale height of the atmosphere is roughly 12 km. Under clear atmosphere, temperature in a lower part of the Martian atmosphere decreases with elevation as in the Earth's troposphere. Because dust directly absorbs Sun's radiation, the more the dust concentrates, the more isothermal is the vertical profile. In other season without dust storms, wind is typically a few meters per second. Wind velocity is often strengthened by local topography and global circulation.

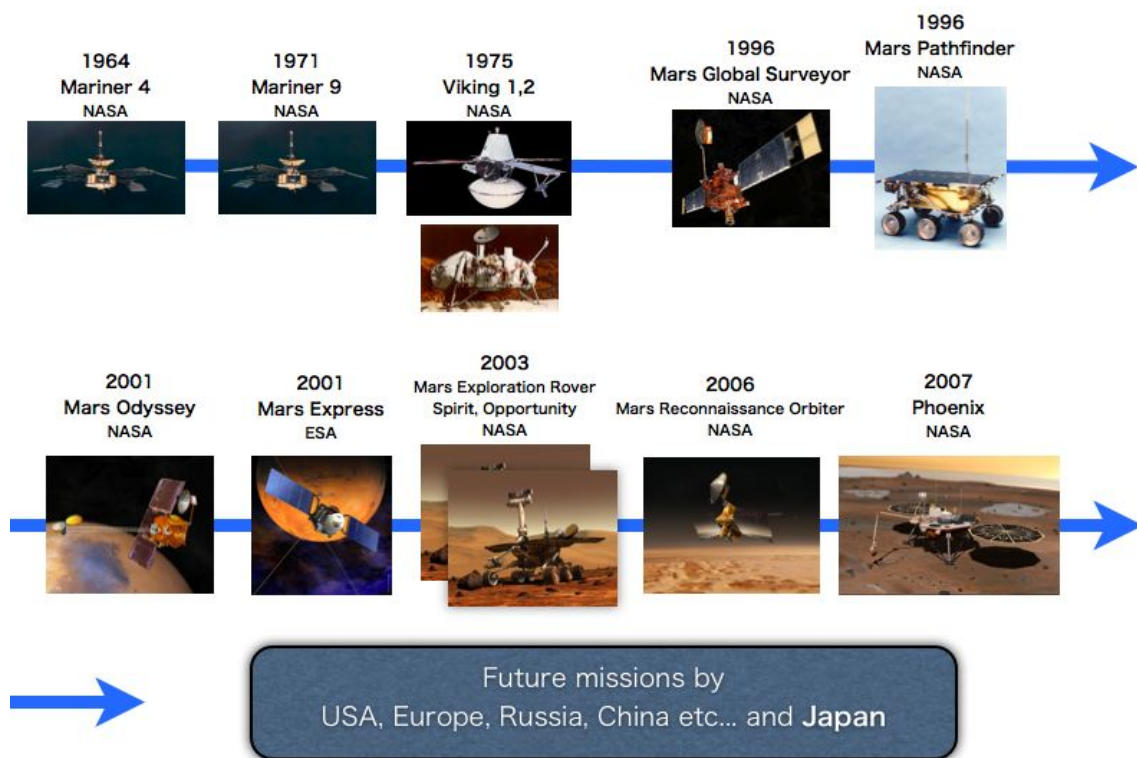


Figure 2: Past spacecraft missions to Mars. (Images are from NASA: <http://www.nasa.gov/> and ESA: <http://www.esa.int/esaCP/index.html>)

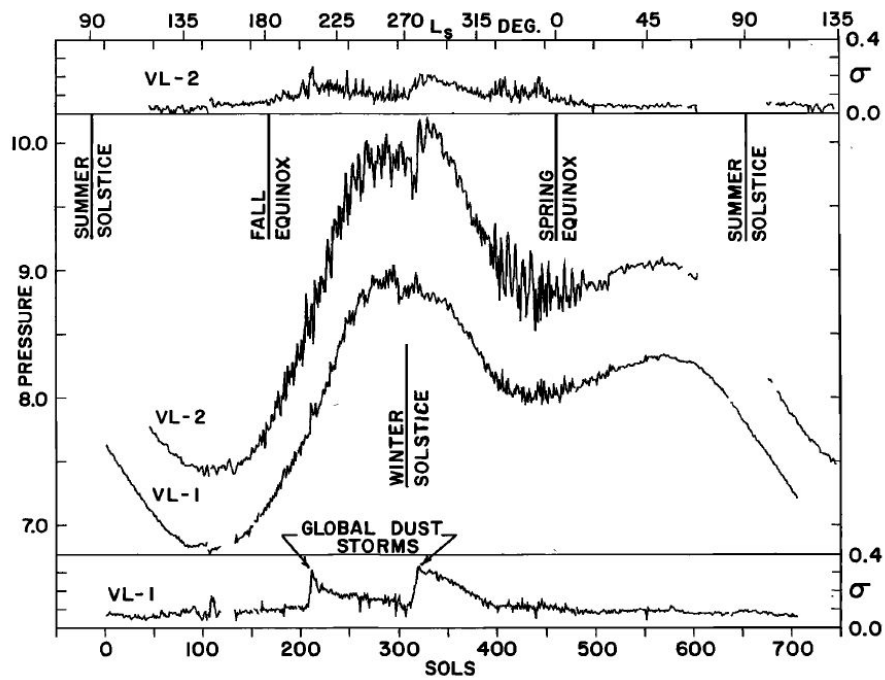


Figure 3: Center block: Daily mean pressures at the two Viking landers for 700sols. Upper and lower blocks: standard deviations of pressure within each sol. All pressures and standard deviations are in mb. The abscissa is time measured in VL-1 sols. The scale labeled  $L_s$  is the areocentric longitude of the sun. The dates of initiation of two global dust storms are marked. Gaps are due to irretrievably lost data. [Hess et al., 1980]

## Dust

Much of the surface is deeply covered by dust, which is mostly composed of fine iron (III) oxide. Winds often lift dust particles into the atmosphere, transporting them around the planet. Local, regional, and global dust storms (Figure 4) are obvious manifestations of the dust transport. Observations of dust devils [Greeley et al., 2006] and atmospheric dust [Smith et al., 2000] indicate that transport of fine-grained particles occurs continuously. Dust particles are estimated to typically be  $<40 \mu\text{m}$  diameter and composed of mostly ferric oxides.

Wind transports materials from one location to another and causes both deposition and erosion on Mars. Depending on a wind speed and density of a planet's atmosphere, there exist three models of the transportation: suspension, saltation and creep (Figure 5). Finer dust is transported by suspension while coarser sand is transported largely by saltation.

Bright and dark wind streaks are examples of features resulting from dust deposition/erosion (Figure 6, 7). Fine-grained dust appears brighter than coarse-grained materials [Wells et al., 1984]. Reflectance of the bright region of Mars is similar to that of a dust ( $< 40 \mu\text{m}$ ) layer, and reflectance of the dark region of Mars is similar to that of a layer of coarser (150 to 250  $\mu\text{m}$ ) materials (Figure 8). Bright streaks are often formed in the downwind direction of topographic obstacles such as impact craters. Dust remains in the lee side of a topographic obstacles, and removed at the surrounding region. Otherwise, topographic obstacles provide regions of reduced winds that allow more dust particles to settle out. Dark wind streaks can be either depositional (composed of dark materials) or erosional due to atmospheric turbulence behind an obstacle.

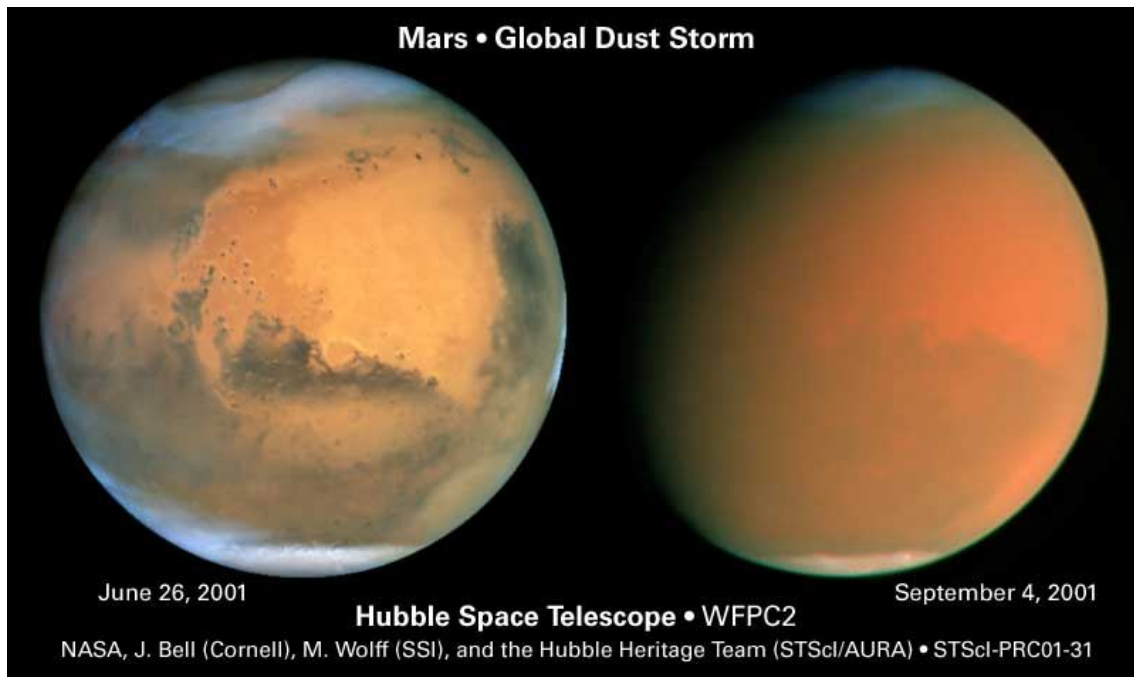


Figure 4: Global Dust Storm (GDS) on Mars. These Hubble Space Telescope images show the Red Planet before (left) and during (right) the great Martian dust storm of 2001 (Image credit: NASA).

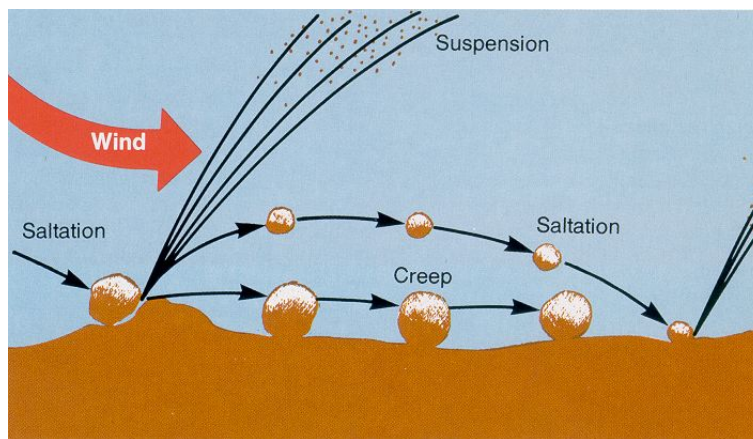


Figure 5: Diagram show in three principal modes of aeolian transport of grains: surface shear stress exerted by the wind causes grain to lift off the surface, carries it downwind back to the surface where it bounces back into flight; this motion is termed saltation. When grain strikes a surface containing very fine particles, then fine particles spray them into the wind where they are carried by turbulence in suspension. Transportation of a particle by pushing downwind a short distance is termed creep (image is from <http://www.weru.ksu.edu/weps/wepshome.html>).



Figure 6: Example of dark depositional streak on Mars (THEMIS Art 17 released 24 Feb. 2004).

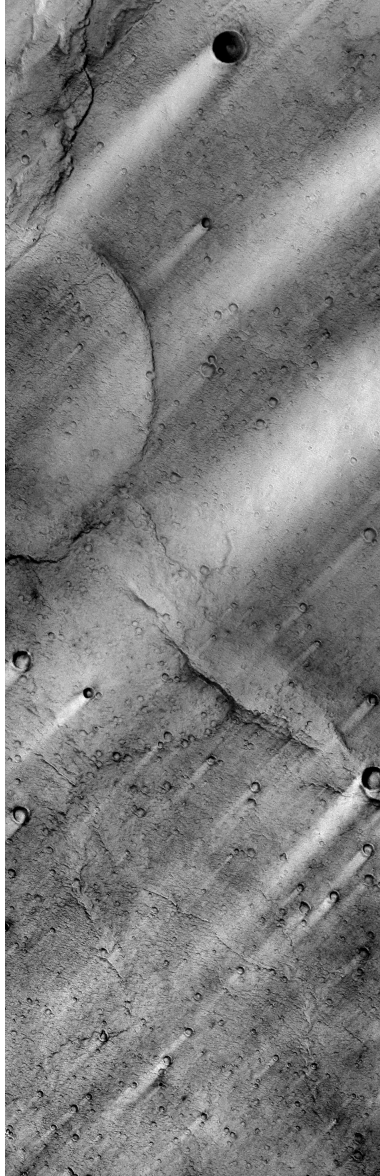


Figure 7: Example of bright streak on Mars (THEMIS Art released 6 June 2002).

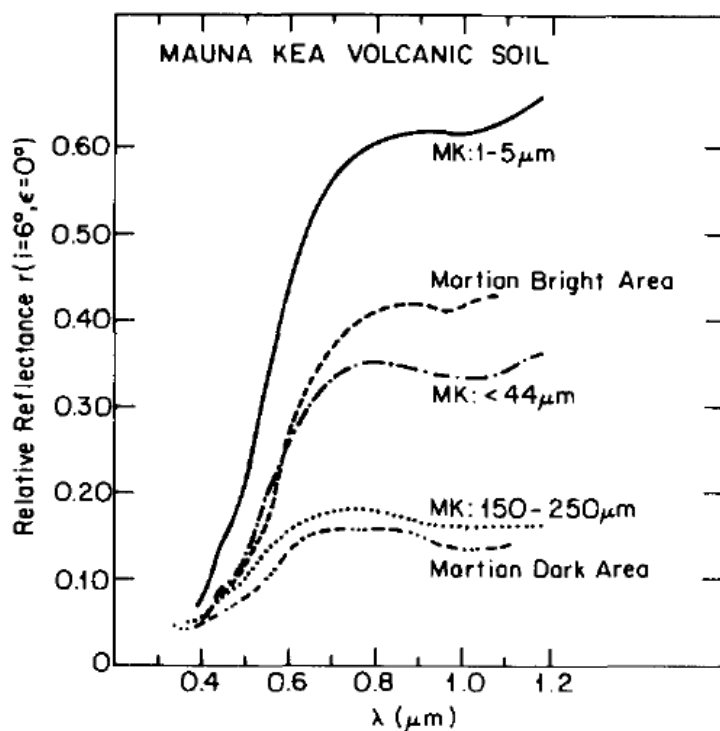


Figure 8: Spectra of different particle size tractions of Mauna Kea soil compared to Martian bright and dark areas from [McCord and Westphal, 1971] at phase angle of 5 deg. The laboratory spectra were taken in wavelength-steps of  $0.03 \mu\text{m}$  [Wells et al., 1984].

## Stability of volatiles

The water content of the atmosphere ranged from less than 1  $\mu\text{m}$  (i.e. if all the water precipitated out of the atmosphere it would form a layer 1  $\mu\text{m}$  deep) over the carbon dioxide caps to 100  $\mu\text{m}$  over the residual northern summer ice cap [Farmer et al., 1977]. If the atmosphere is well mixed, partial pressures of water at the surface range from  $10^{-6}$  to  $10^{-5}$  bars, 2-3 orders of magnitude short of the 6.1 mbars needed to stabilize liquid water [Carr, 2006].

Despite its thermodynamic instability, liquid water could occur transiently near the surface today under certain conditions. Over most of the planet, any water brought to the surface would rapidly boil or freeze. However, liquid water might transiently exist at mid to high latitudes because of the presence of ice in the soil and greater penetration of the diurnal thermal wave in summer. Water ice is stable just below the surface at high latitudes.

Carbon dioxide is usually gas on Mars, but can be solid in some region such as polar cap. Rheological, thermal, and spectroscopic properties indicate that the south polar permanent cap is composed of water ice covered by an 8-m-thick veneer of carbon dioxide ice [Nye et al., 2000; Titus et al., 2003; Bibring et al., 2004].

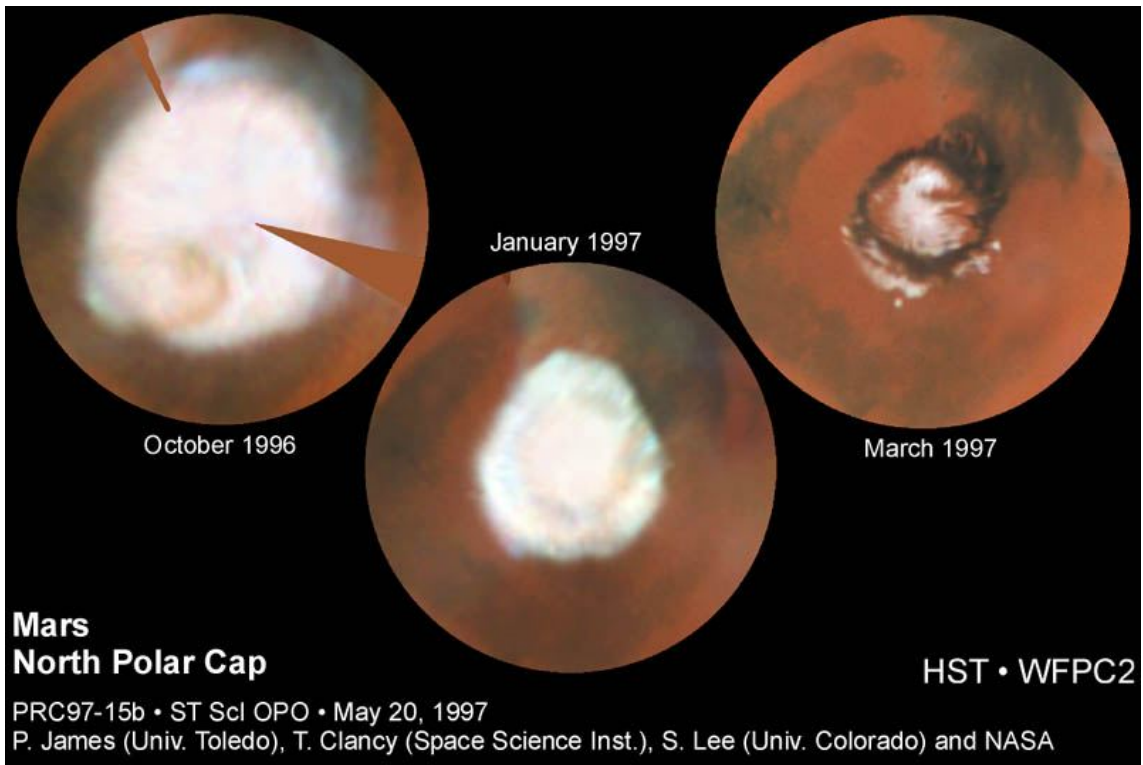


Figure 9: North polar cap of Mars, taken by Hubble Space Telescope.

### 1.1.3 Volcanism on Tharsis

There are two most prominent volcanic provinces; Tharsis and Elysium. The Tharsis Montes narrowly refers to the line of three large volcanoes, Arsia Mons, Ascreus Mons, and Pavonis Mons. The name Tharsis is commonly used in a more general sense to refer to a broad region of anomalously high elevations centered just south of the equator. Although almost the whole bulge is covered by post-Noachian lava plains, the individual volcanoes are distributed unevenly.

The three aforementioned volcanoes together with Ceraunius Tholus and Uranus Patera form a SW-NE trending line that cuts across Tharsis. The SW-NE line is clearly a major structural feature of the planet whose origin remains obscure. [Zhong, 2009] proposed "rotating shell model" to explain migration of volcanism in Tharsis region. Zhong proposes that the entire martian lithosphere moved relative to the underlying mantle: this can explain why Tharsis now lies at the boundary between the northern and southern hemispheres and also how the volcanism in this region migrated. This idea could be responsible for formation of the SW-NE trending line.

In this thesis, dark streaks on Pavonis Mons are investigated. Pavonis Mons is located at the middle volcano of the three large Tharsis Montes, is somewhat smaller than the other two, being 14 km high and having a volume of  $4 \times 10^5 \text{ km}^3$ . The summit caldera, almost 5 km deep, is inset into a larger older depression, now almost filled.

## 1.2 Introduction to this thesis

Parameters near the surface of Mars are hard to investigate with satellite-based remote sensing systems. For example, wind velocity near the surface was measured only at a few landed sites of landers. Such surface parameters are indispensable to understand martian environment deeply. Surface parameters are also essential as checking points of the Mars Global Circulation Models (MGCs).

Images taken by spacecrafts could be useful tools to estimate the environmental parameters near the surface of Mars. Such images cover entire region of Mars, and they would give us global information on the surface. Interactions between the atmosphere and the ground surface cause observable changes in the surface pattern. Therefore, we can understand the surface environment by investigating surface patterns seen in the images.

In this Thesis, a time-variable surface pattern called "Dark Halo" is investigated. "Dark Halo" is a new kind of pattern near the top of high altitude volcanoes in Tharsis region (Figure 10), and shows temporal changes in its pattern (Figure 11). "Dark Halo" might bring us important information of the changing surface environment at Martian volcanoes.

In following sub-sections of this section, present interpretation of low albedo feature and wind streak on Mars will be introduced firstly. Secondly, the characteristic of "Dark Halo" will be described. Lastly, Enigmas of "Dark Halo" and problems to be resolved by this thesis will be presented. In section 2, instruments and data, used to investigate "Dark Halo" in this thesis, will be introduced. In section 3, morphological features and temporal changes of "Dark Halo" derived from data of the instruments will be investigated. In section 4, possible interpretations for the results of our investigation will be discussed. In section 5 and the rest sections, conclusion, summary and future work will be presented.

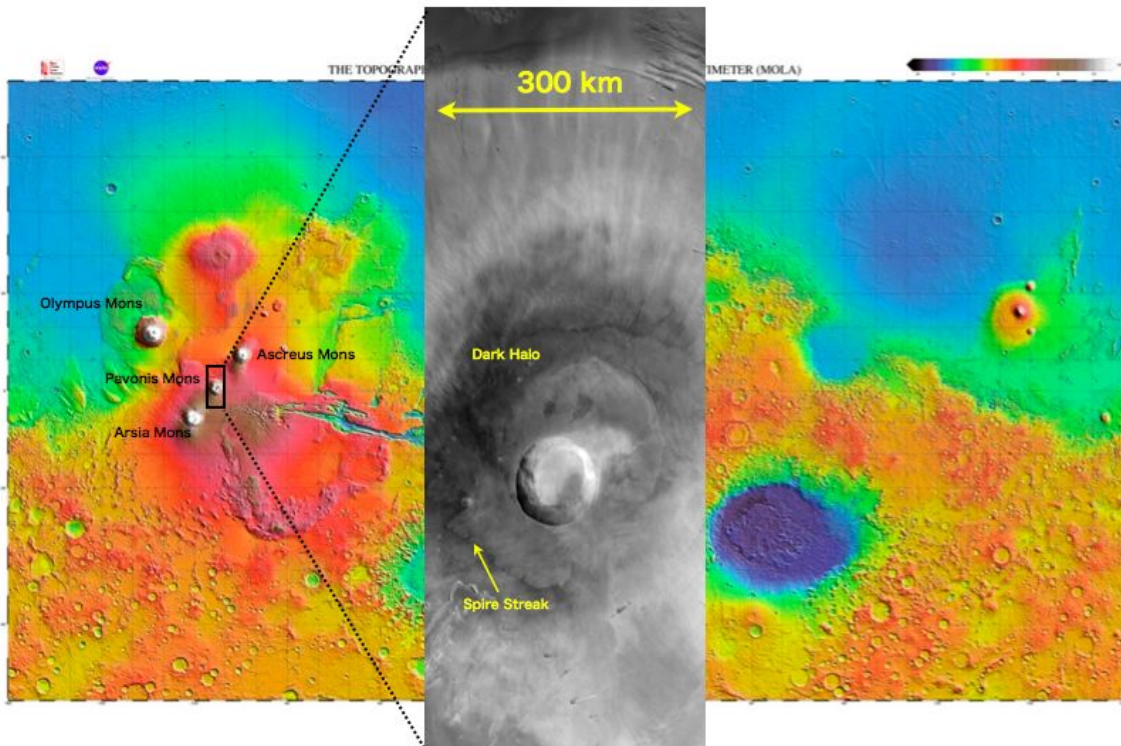


Figure 10: "Dark Halo" on a Martian volcano. Mars Global Surveyor (MGS) Mars Orbiter Camera (MOC) took the image at center. The topography map behind is from MGS Mars Orbiter Laser Altimeter (MOLA).

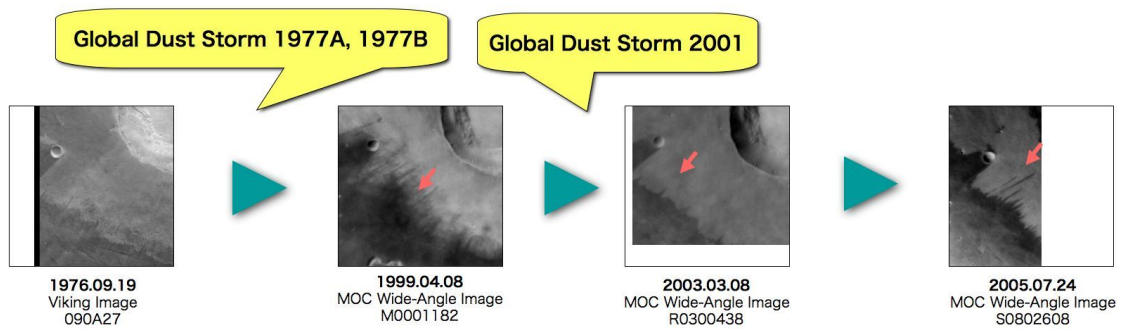


Figure 11: "Dark Halo" and its variations taken by MGS MOC and Viking orbiter.

### 1.2.1 Cause for low albedo on Mars

The dark regions (the albedo is lower than 0.2 or so) on Mars have long been recognized, first by astronomers and more recently, by investigators using instruments on spacecrafts. The classical dark features are relatively dust-free but are still dominated by particulate materials ranging from 0.1 mm to 1 cm [Christensen and Moore, 1992] rather than bedrock. Compositionally, dark regions appear to be dominated by minerals found in mafic volcanic rocks, specifically, pyroxene [e.g., Singer et al., 1979; Mustard et al., 1993; Bell et al., 1997; Bandfield et al., 2000a; Christensen et al., 2000a]. These results are consistent with direct observations by rovers [Greeley et al., 2005; Geissler et al., 2008].

[Putzig et al., 2005] considered the quantitative comparison of thermal inertia and albedo, which is used to delineate the Martian surface by thermophysical properties. Table 1 lists the ranges in thermal inertia and albedo and their interpretation for each unit. Figure 12 shows spatial distribution of the units on the surface of Mars. Tharsis region, investigated in this thesis, belongs to the Unit A or G. Unit A, Unit G probably represents deposits of the fine dust. Those portions of Unit G with higher thermal inertia may represent a cover of dust which is thermally thin (less a skin depth, i.e., a few cm) over material that might otherwise display the characteristics of the surrounding Units C and F.

Table 1:

| Mars thermal inertia–albedo units |                   |                      |           |                                          |
|-----------------------------------|-------------------|----------------------|-----------|------------------------------------------|
| Unit                              | Inertia           | Albedo               | % surface | Interpretation                           |
| A                                 | Low (28–135)      | High (0.23–0.31)     | 19        | Bright unconsolidated fines              |
| B                                 | High (160–355)    | Low (0.10–0.19)      | 36        | Sand, rocks, and bedrock; some duricrust |
| C                                 | High (110–330)    | Med. (0.19–0.26)     | 23        | Duricrust; some sand, rocks and bedrock  |
| D                                 | Low (24–170)      | Low–med. (0.09–0.24) | 2         | Low density mantle <i>or</i> dark dust?  |
| E                                 | High (140–386)    | Very Low (< 0.09)    | 0.3       | As B, but little or no fines             |
| F                                 | Very high (> 386) | All                  | 4         | Rocks, bedrock, duricrust, and polar ice |
| G                                 | Low–high (40–386) | Very high (> 0.23)   | 0.7       | As A, thermally thin at higher inertia   |

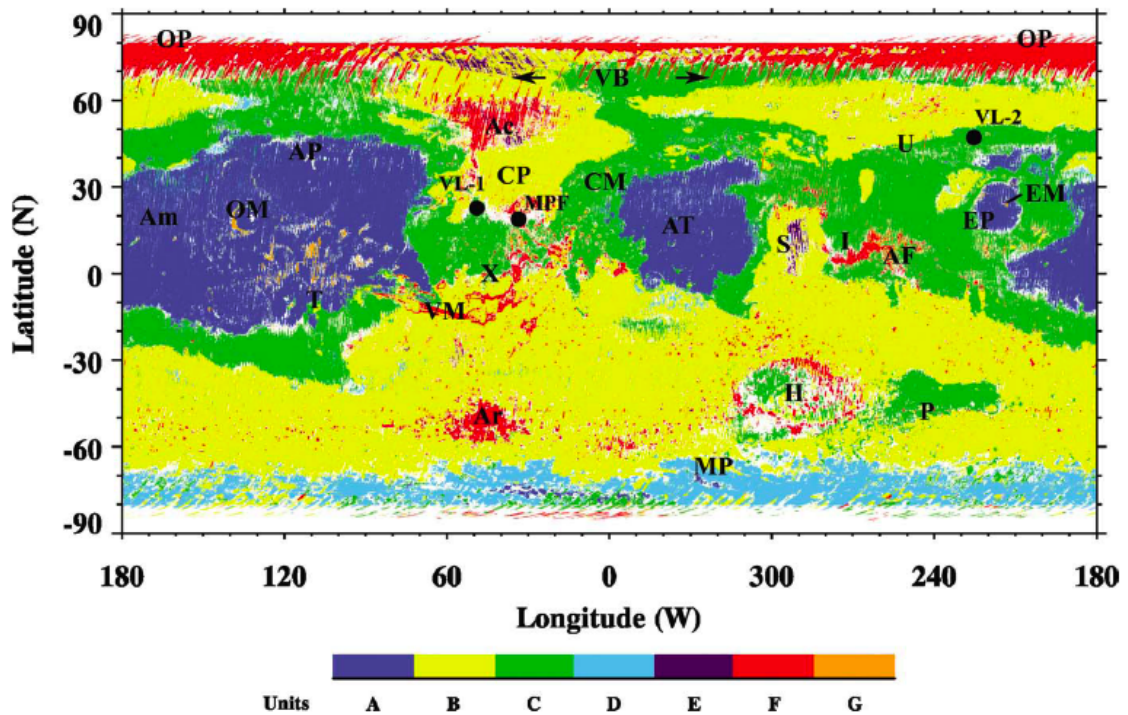


Figure 12: Thermal inertia–albedo unit map of Mars [Putzig et al, 2005]. Units represent thermal inertia–albedo modes summarized in Table 1. Lander locations and regions: VL–1, Viking Lander 1; VL–2, Viking Lander 2; MPF, Mars Pathfinder Lander; Ac, Acidalia; AF, Amenthes Fossae; Am, Amazonis; AP, Alba Patera; Ar, Argyre; AT, Arabia Terra; CP, Chryse Planitia; CM, Cydonia Mensae; EM, Elysium Mons; EP, Elysium Planitia; H, Hellas; I, Isidis; MP, Malea Planum; P, Promethei Terra; OM, Olympus Mons; OP, Olympia Planitia; S, Syrtis Major; T, Tharsis; U, Utopia Planitia; VB, Vastitas Borealis; VM, Valles Marineris; X, Xanthe Terra.

## **1.2.2 Wind streaks on Mars**

On the planets having atmosphere such as Mars, there are various types of interactions between the atmosphere and the ground surface. Such interactions cause observable changes in the surface patterns. Wind streaks are typical examples.

### **Bright wind streaks**

The Martian wind streaks are basically classified into two categories depending on the relative albedo change from the background [e.g. Veverka et al., 1981; Greeley et al., 1985].

- (1) Bright depositional streaks: deposits of wind-blown materials having higher albedo. Since the deposition process is controlled by the relative importance of the settling velocity over the lateral wind velocity, efficient deposition is expected at place of weak wind. Bright depositional streaks are probably formed during global dust storms: topographic obstacles provide regions of reduced winds that allow more dust particles to settle out.
- (2) Bright erosional streaks: the place where coarser grained particles are removed from surface that is initially covered with a mixture of fine-grained and medium-grained particles (Figure 13 (B)). Bright erosional streaks might be formed under strong wind because finer particles need higher wind velocity to move.

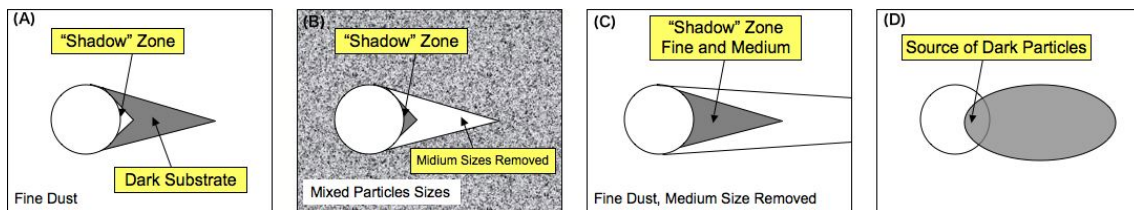


Figure 13: Diagrams showing some possible origins of light and dark streaks (revised version based on [Greeley and Iversen, 1985]). (A) the entire surface is covered with fine dust; dust is later removed in the wake of the crater as a result of preferential erosion to expose a dark substrate; (B) the surface is initially covered with a mixture of fine-grained (high-albedo) and medium-grained (low-albedo) particles; medium-grained particles are easier to move by the wind than fine-grained ones, thus, the medium-grained particles are removed from the wake zone at the crater, leaving the fines that appear as a high-albedo zone; (C) the crater is a source for the dark particles that are carried by the wind downstream and deposited as a plume; these are probably rather rare on Mars; (D) under very high winds, the 'shadow zone' in the immediate lee of the crater may lengthen; it would consist of medium- and fine-grained particles (low-energy zone) and would appear relatively dark in comparison to the surrounding terrain where the medium-grained particles would have been removed. Particle are defined as follows (based on threshold curves conducted under martian surface pressures): (A) fine,  $< 40\mu\text{m}$ , (B) medium,  $40\text{-}600\mu\text{m}$ , (C) coarse,  $> 600\mu\text{m}$  (from [Greeley et al., 1987]).

## **Dark wind streaks**

Dark wind streaks are also classified into two categories [Thomas et al., 1981]. (1) Dark streaks with no source deposit: interpreted to be formed by erosion of dust. (2) Dark streaks associated with deposits of sediment: interpreted to be formed by deposition of dark material moved by saltation. The orientations of these wind streaks reflect both global flow patterns and slope-controlled winds. Figure 13 shows schematic diagrams of some possible origins of light and dark streaks, and category (1) and (2) are shown in Figure 13 (A, C) and (D) respectively.

Erosional dark streaks need stronger wind than depositional dark streaks to remove fine dust from the surface [Veverka et al., 1981]. Only in restricted areas where wind stress on the surface is increased sufficiently by topography, effective removal of the surface materials can happen. Seasonal variations of erosional dark streaks are associated with seasonal variations of wind velocity [Peterfreund, 1981]. Thermal inertia of erosional dark wind streaks is distinct from the surroundings, indicating presence of sand-sized particles thicker than a few centimeters [Pelkey et al., 2001]. Dark surface streaks are considered similar to the dust devil tracks, which are formed by removal of the surface dust after the passage of dust devils.

## **Coalesced streaks**

Coalesced dark streaks are found in Tharsis and Syrtis Major [Thomas et al., 1981; Lee et al., 1982] (Figure 14). All four Tharsis Volcanoes has the prominent dark collars, called "Dark Halo" in this thesis, and were thought to be kinds of coalesced dark streak. Other occurrences of coalesced dark streaks are found on the plains surrounding the major volcanoes. Coalesced dark streaks occur only in small areas of Elysium. A dark collar is present at the summit of Elysium Mons. Coalesced streaks are thought to be kinds of wind streaks. However, no further detailed study has been done on coalesced streaks. Coalesced dark streaks have been detected to be variable through a dust storm [Peterfreund, 1981].



Figure 14: Coalesced streaks in Syria Planum. This image was taken by Viking orbiter, and reference number is 648A06 [Thomas et al., 1981].

### **1.2.3 "Dark Halo" at high altitude volcanoes**

"Dark Halo" is first described in detail by [Sagan et al., 1974]. They interpreted it as a kind of a wind streak pattern, an aeolian product. Following researches [Thomas et al., 1981; Lee et al., 1982; Thomas et al., 1984; Thomas et al., 2003] took over their idea, and suggested contributions of roles of the boundary layer and surface material interaction with the atmosphere. Dark albedo features such as "Dark Halo" has been thought to be kinds of coalesced streaks and to exist universally near the top of high mountains (Olympus, Elysium, Pavonis and Ascraeus) [Sagan et al., 1974].

#### **Recent studies on "Dark Halo" of Pavonis Mons**

[Sagan et al., 1974] interpreted "Dark Halo" as a track of aeolian transportation of fine-grained particles. Since they estimated the atmospheric pressure on the summit of Pavonis Mons to be  $< 200$  Pa, minimum wind velocities to move fine dust and form "Dark Halo" were estimated to be about 110 m/s above the surface boundary layer. [Lee et al., 1982] interpreted "Dark Halo" as a kind of coalesced streak, and they thought that "Dark Halo" is an prominent example of dust erosion induced by slope winds. [Lee et al., 1982] also found that neighboring crater-related streaks are oriented downslope. They thought some portion of the dust raised by downslope winds is redeposited shortly thereafter on the lower flanks of Pavonis Mons. Previous studies considered "Dark Halo" to be an ordinary erosional pattern.

#### **Enigmatic features of "Dark Halo"**

After [Lee et al., 1982], there is no careful study on the origin of "Dark Halo". Therefore, recent high-resolution images (e.g. MOC, THEMIS, HRSC, HiRISE and CTX) are not investigated for "Dark Halo". In such high-resolution images, we can see enigmatic features of "Dark Halo":

1. "Dark Halo" is composed of assemblage of dark spire-shaped streaks, hereafter we call "Spire Streaks" (Fig 30).
2. Each streak starts from a point-like very narrow region.
3. In most cases, no topographical obstacle can be identified neither at the initiation point nor at the wider side of "Spire Streak" even in a recent high-resolution image.
4. Each "Spire Streak" starts at high position and increases its width downward.

5. "Spire Streak" shows temporal changes in its pattern as "Dark Halo" (Figure 11).

"Spire Streak" might not be an ordinary dark depositional wind streak because any source of dark material that form dark "Spire Streak" can't be found around "Spire Streak". "Spire Streak" might not be an ordinary dark erosional wind streak because the spindle-shape of "Spire Streak" needs topographic obstacles to be formed. These features seem to be incompatible with existing models of aeolian streaks. In this thesis, we focus those 5 points through the analysis of recent high-resolution images and compare the shape of spire streaks in detail with models for the formation of aeolian streaks.

#### **1.2.4 Problems to be resolved in this thesis**

It is the purpose of this thesis to determine relative importance of factors affecting the formation of "Spire Streak". Characteristics of the regions where "Spire Streak" occurs are deduced from visible/IR images, spectral data and data of a numerical modeling. Of particular interest in this study is the reason why the shape of "Spire Streak" changes, as this should reflect near-surface environment that is hard to investigate with satellite-based remote sensing systems. Results of these investigations will re-define "Dark Halo" itself.

## 2 Method

### 2.1 Numerical modeling of surface pressure

Today, General Circulation Models of Mars can reproduce Martian climate parameters such as pressure, temperature and wind velocity. In this thesis, a numerical modeling for surface pressure of Mars by Haberle and Wilson (Mars General Circulation Modeling Group of NASA) was used to estimate the surface pressure.

### 2.2 Laser Altimeter

The Mars Orbiter Laser Altimeter (MOLA) onboard Mars Global Surveyor (MGS) provided accurate global topographic map of Mars (Figure 15) within the nominal precision of about 1 m in the vertical dimension [Zuber et al., 1992]. In this thesis, Mission Experiment Gridded Data Records (MEGDRs) of MOLA is used to investigate topographic features at the dark halo.

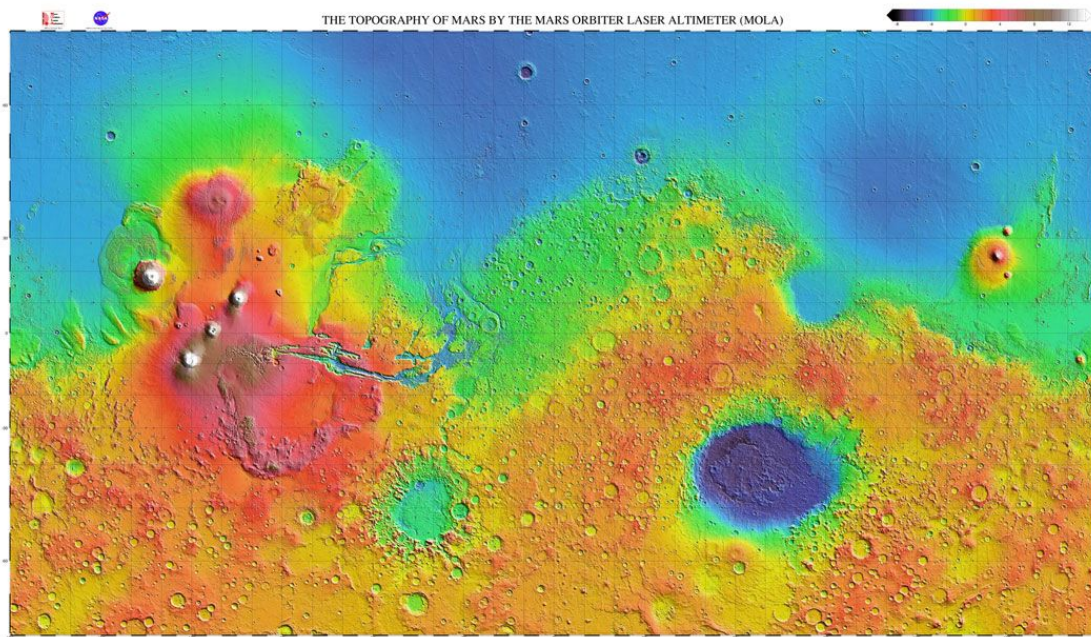


Figure 15: Topographic shaded relief map of Mars derived from MOLA observation. [NASA]

### 2.3 Visible imagers

Images from Viking orbiter, Mars Global Surveyor (MGS) Mars Orbiter Camera (MOC), Mars Odyssey Thermal Emission Imaging System (THEMIS), Mars Express High Resolution Stereo Camera (HRSC), Mars Reconnaissance Orbiter (MRO) High Resolution Imaging Science Experiment (HiRISE) and Context Camera (CTX) were examined for the dark halo on Pavonis Mons. Table 2 summarizes basic characteristics of the instruments (the characteristics are from [Thorpe, 1976; Christensen et al., 2004; Malin et al., 2007; Mcewen et al., 2007] and web pages of NASA: <http://www.nasa.gov/> and ESA: <http://www.esa.int/esaCP/index.html>). Figure 16 - 18, and 20 are examples of images that were obtained by the instruments.

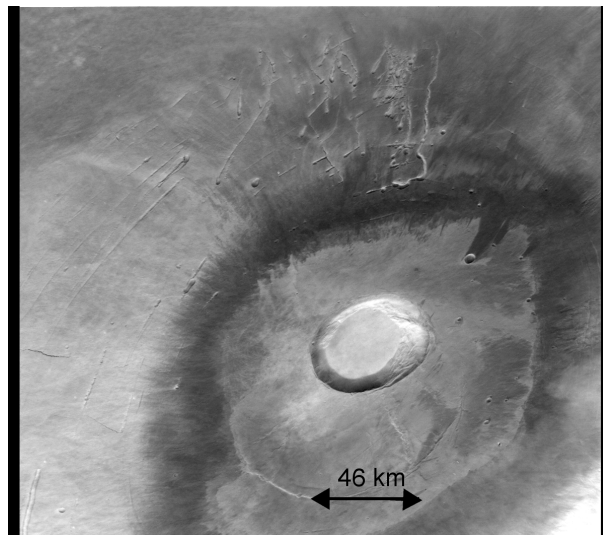


Figure 16: Image taken by Viking Visual Imaging Subsystem Camera A (052A15).

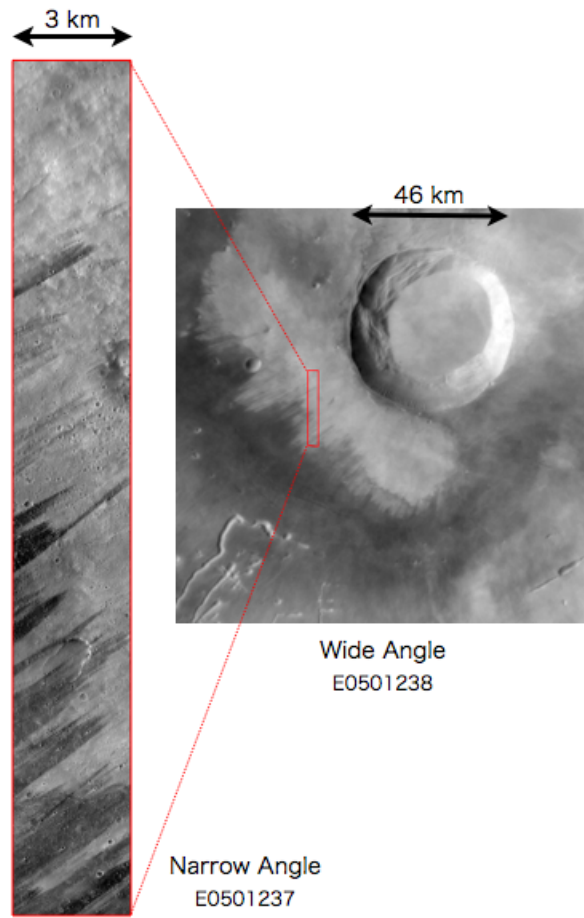


Figure 17: Images taken by Mars Orbiter Camera onboard Mars Global Surveyor.

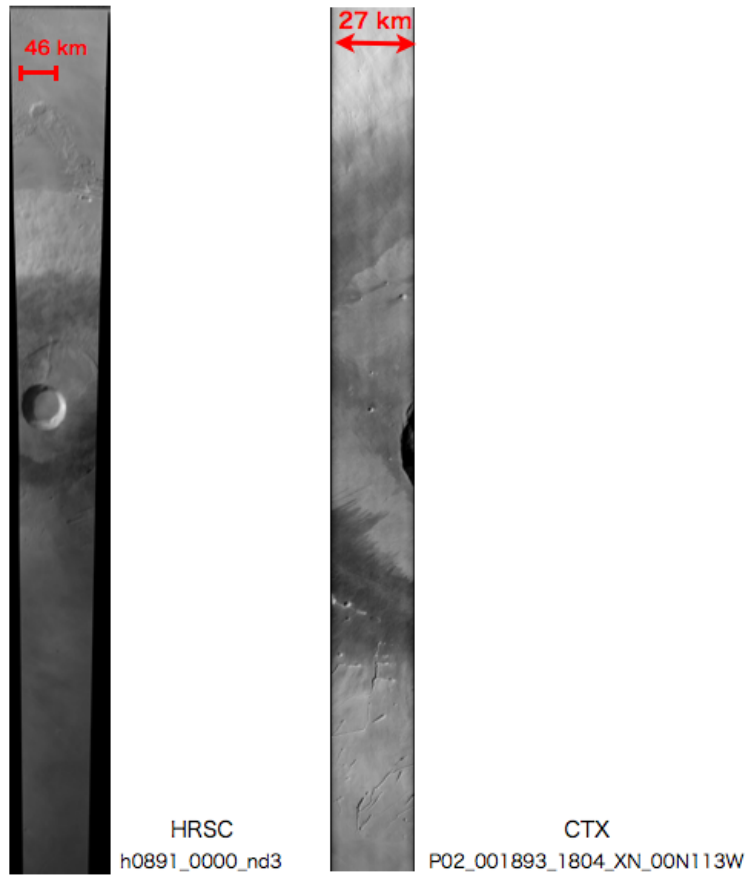


Figure 18: Images taken by HRSC (onboard Mars Express) and CTX (onboard Mars Reconnaissance Orbiter).

Table 2: Visible imagers onboard spacecrafts

| Instrument             | Viking Orbiter Camera | MOC Wide Angle                        | Mars Global Surveyor | MOC Narrow Angle | THEMIS VIS                | HRSC                                   | HiRISE                                                | CTX        |
|------------------------|-----------------------|---------------------------------------|----------------------|------------------|---------------------------|----------------------------------------|-------------------------------------------------------|------------|
| Spacecraft             | Viking Orbiter        |                                       |                      |                  |                           |                                        |                                                       |            |
| Radiometric resolution | 8 bit                 | 8 bit                                 | 8 bit                | 8 bit            | Mars Odyssey<br>8 bit     | Mars Express<br>8 bit                  | Mars Reconnaissance Orbiter<br>14 bit                 | 12 bit     |
| Spectral band pass     | 444-1050 nm           | 575-625 nm (Red)<br>400-450 nm (Blue) | 500-900 nm           | 420-860 nm       | 585-765 nm<br>925-1015 nm | 730-770 nm<br>485-575 nm<br>395-485 nm | 570 - 830 nm (Red)<br>< 530 nm (BG)<br>> 790 nm (NIR) | 500-800 nm |
| Spatial resolution     | 90-200 m/pixel        | 230 m/pixel                           | 1.41 m/pixel         | 18 m/pixel       | 10 m/pixel                | 30 cm/pixel                            | 6 m/pixel                                             |            |

## 2.4 Imaging spectrometers

An imaging spectrometer is useful to investigate physical and mineralogical characteristics of planetary surface. Figure 19 is a schematic representation of data of imaging spectrometer. Imaging spectrometer can obtain spectral image "cube" that gives us spatial and spectral information at the same time. Table 3 summarizes basic specs of imaging spectrometers onboard spacecrafts to Mars (the specs are from [Christensen et al., 1992, 2004; Murchie et al., 2007] and the web page of ESA: <http://www.esa.int/esaCP/index.html>).

In this thesis, MGS Thermal Emission Spectrometer (TES) and Mars Odyssey Thermal Emission Imaging System (THEMIS) are investigated for the dark halo. Dust Cover Index (DCI) [Ruff and Christensen, 2002] and thermal inertial [Putzig et al, 2005] is obtained from TES data. Brightness temperature of the surface is obtained from THEMIS data. Figure 20 is an example of THEMIS images.

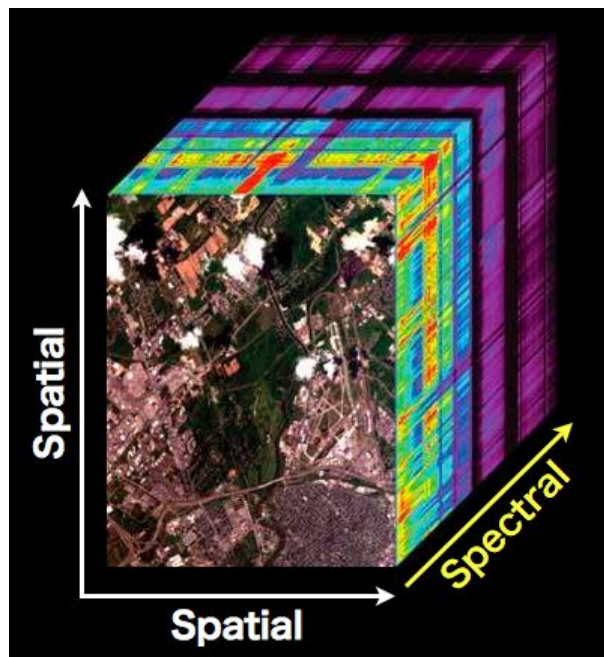


Figure 19: An airborne image, with its spectrum shown as a colored stack beneath each pixel, creates a three-dimensional image cube that emphasizes the spectral nature of the data. (Image credit: NASA Jet Propulsion Laboratory)

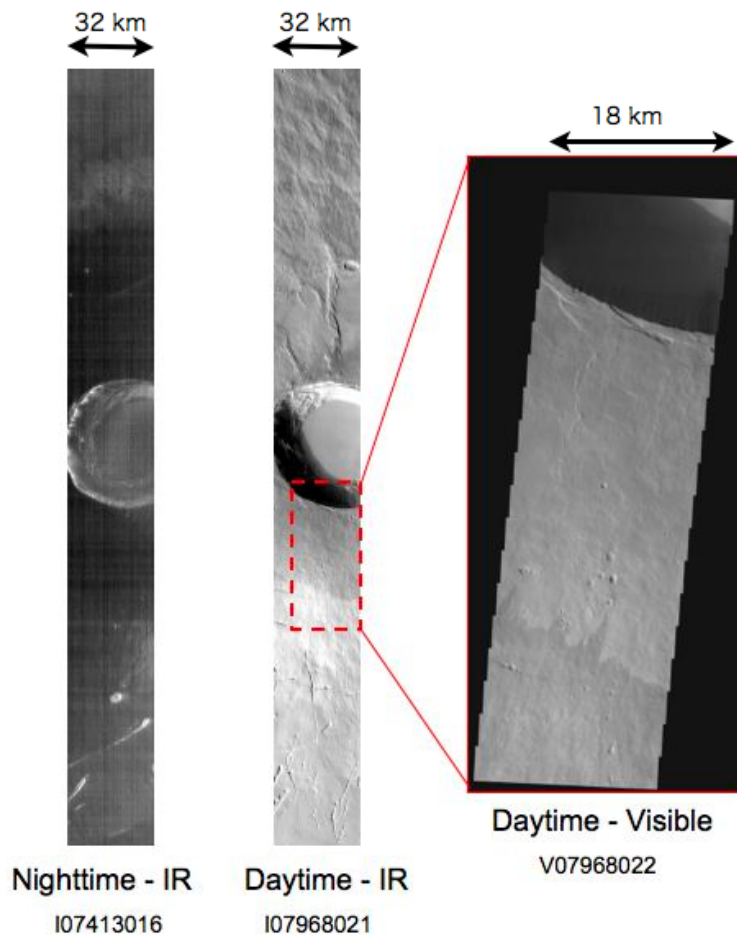


Figure 20: Images taken by THEMIS onboard 2001 Mars Odyssey.

Table 3: Imaging spectrometers onboard spacecrafts

| Instrument             | TES                                         | THEMIS IR                              | OMEGA                  | CRISM                       |
|------------------------|---------------------------------------------|----------------------------------------|------------------------|-----------------------------|
| Spacecraft             | Mars Global Surveyor                        | Mars Odyssey                           | Mars Express           | Mars Reconnaissance Orbiter |
| Radiometric resolution | 8 bit                                       | 8 bit                                  | 12 bit                 | 14 bit                      |
| Spectral range         | 6-50 $\mu\text{m}$<br>0.3-2.9 $\mu\text{m}$ | 6.8-14.9 $\mu\text{m}$                 | 0.36-5.2 $\mu\text{m}$ | 0.36-3.9 $\mu\text{m}$      |
| Spectral resolution    | 0.05-0.1 $\mu\text{m}$                      | 1-10 $\mu\text{m}$ (9 different bands) | 7.5-20 nm              | 6.6 nm                      |
| Spatial resolution     | 3 km/pixel                                  | 100 m/pixel                            | 100 m/pixel            | 18-36 m/pixel               |

## 3 Results

### 3.1 Morphology and distributions

#### Dark halo

The dark halo is found on high slope region of the mountain edifice (Figure 21). This feature is also seen on other volcanoes in Tharsis. Figure (22, 23, 24) shows elevation map of Olympus, Ascreus and Arsia Mons respectively, and dark halo is also found on the high slope region same as Pavonis Mons. Flank slopes that were derived from MEG-DRs by [Plescia, 2004] are summarized in Table 4. The upper boundary which is a rim of the dark halo at higher altitude close to the summit, can be identified easily because of the high contrast of albedo, while the lower boundary is more or less vague because of low contrast. The albedo is also not homogeneous in the dark halo (Figure 25). On Olympus and Pavonis Mons, the upper boundary of the dark halo seems to be at inflection-point of slope. This tendency is seen in any directions of the cross-sections at both volcanoes. In most cases the albedo becomes lower towards the upper boundary, which makes identification of the upper boundary easy. The dark halo of Ascreus and Arsia Mons looks different from that of Olympus and Pavonis Mons. The place of the upper boundary of dark halo is not only at inflection-point of the slope. This difference is probably due to the difference of the mountain edifice. For example, Olympus and Pavonis have the flat area at the their summit, though Ascreus and Arsia don't have such large flat area. Wind direction might vary because of such differences of the topography. The global circulation might also cause variations of wind directions and affect the shape of the dark halo. Height of the upper and lower boundary of the dark halo at Tharsis volcanoes are summarized in Table 4. Surface pressure might not play an important role to form the dark halo, because the heights of the upper boundaries are different from each other.

The dark halo shows different appearance in visible, nighttime and daytime infrared images (Figure 20). The dark halo is found as a dark albedo feature in visible images. In daytime infrared images, the dark halo is found as a brighter feature, which means higher temperature. On the other hand, the dark halo cannot be recognized in nighttime infrared images. This means there exist no temperature difference between the dark halo and the surrounding region at nighttime. These features are indicated at the same time in Figure 26. The lowest part of Figure 26 displays a daytime IR image of Pavonis Mons which is shown on MOC global mosaic. The elevation topography of Pavonis Mons and brightness temperature derived from the IR image are shown at the middle and highest

part of Figure 26 respectively. The right side of Figure 26 is sunny side, and the left side is shadow area at the shooting time of the IR image. The dark halo looks brighter (i.e. higher temperature) at the sunny side, while there seems to be no difference in temperature between the dark halo and its surrounding region at the shadow area. The shadow area has similar distribution of temperature as that of at nighttime.

Variation of the thermal inertia of the surface material is one of the major factors controlling the surface temperature. Temperature difference between the dark halo and its surroundings is shown in Figure 44. If the thermal inertia at the dark halo is as low as 200, the temperature should be higher at daytime and should be lower at nighttime than that of the surrounding area. The effect of thermal inertia and albedo on diurnal variations of the surface temperature was shown in Figure 27. The low albedo feature can increase surface temperature both at daytime and at nighttime (though the increase of temperature is smaller at nighttime). Low value of thermal inertia can increase daytime surface temperature too, though low thermal inertia decreases nighttime temperature. Since no apparent temperature difference is detected at nighttime, the high temperature at daytime should not be due to the thermal inertia. The low albedo of the dark halo might be responsible for the higher temperature at daytime. The homogeneity of the surface temperature at nighttime is probably because the surface is in thermal equilibrium with the atmosphere at nighttime.

Many bright dust devil tracks (DDTs) are found on the dark halo (Figure 28). DDTs can be seen as brighter tracks both at the dark halo and at surrounding bright region (Figure 29). However that may be, the sub-surface structure is still enigmatic because many dark DDTs on the bright region are also found.

### **Spire Streaks**

If we see the area of the upper boundary in close-up views, we can find the dark halo is an assemblage of many overlapping spire streaks. Spire streaks exist at the boundary between where dark halo can be formed and can't be formed. Therefore, formation process of spire streaks is the same as that of the dark halo.

Morphology of spire streaks is enigmatic. Each spire streak is spindle-shaped with length of 1-10 km and width at the middle part of several hundred meters, and is usually rectilinear (Figure 30). The shape of spire streak cannot be explained with any existing model of wind streak.

Spire streaks can pass over topographic obstacles such as craters (Figure 31 (B) ) This

feature is consistent with depositional origin of the spire streak. Neither DDT nor other erosional process seems to be able to remove surface materials and make a spindle-shaped feature regardless of any topographic obstacles.

There seems to be no related obstacles at the start point of the spire streak (Figure 30). Related obstacles at upstream side of wind are needed to make spindle-shape like the spire streak with existing theory for formation of wind streak. However, there seem to be no related obstacles at the wider side of the spire streak either. Either depositional process (to be discussed in next section) or a new kind of erosional process plays an important role to form spire streak.

Some spire streaks seem to be related to crater at the start point. However, the shape of spire streaks related to craters are not always the same (Figure 31 (A) (C) (D) ). Every “crater related” spire streak doesn't have the point which is the origin of the name “spire streak”. In Figure 31 (A), the streak hardly seems to become wider going away from the crater. In Figure 31 (C), the streak apparently become wider going away from the crater. In Figure 31 (D), the distribution of the “crater related” streaks covers a wide area. The intersection points of the craters with the streaks are different in its width. These differences might reflect the difference of wind surrounding the craters.

Spire streak is found not only at the upper boundary of the dark halo but also in the rim of the caldera of Pavonis Mons (Figure 32 (B)). The max slope direction at the rim of the caldera is caldera-ward. Therefore, presence of spire streaks at the rim of the caldera is consistent with other spire streaks at the high slope region. Spire streak on the rim of the caldera looks dull compared to those on the upper boundary of the dark halo. The difference of the streak sharpness by location probably reflects differences of wind velocity.

Direction of spire streak is usually same as that of bright wind streak which is related to crater (Figure 32 (A)). The directions of bright wind streaks are consistent with the direction of downhill wind. No wind streak that is consistent with uphill wind is found at the dark halo. Therefore, downhill wind has strong effect on the surface pattern at the spire streak and dark halo.

In some regions, we can find spire streaks that have different directions at the same place (Figure 28). In this image, the spire streaks having different orientation are mixedly distributed. One is NNE-SSW trend and the other is NW-SE trend. The NNE-SSW trend is darker than NW-SE trend. The bright wind streaks behind crater having NNE-SSW trend are recognized to erase NW-SE trend streaks. These clearly show NNE-SSW

trend streaks are recent and NW-SE trend streaks are older. This means the wind pattern responsible for the formation of the spire streaks changes with time. The direction of the maximum slope in this image is about N-S so that the NW-SE trend significantly deviates from the direction of the maximum slope.

Spire streaks can be overwritten (Figure 33). Spire streaks don't seem to be formed at night everyday, because there seems to be only a few groups of the spire streaks that have same darkness of albedo. The formation of the spire streak might be an extraordinary process at the surface of the volcano.

Figure 34 is a distribution map of clear spire streaks. Most of the spire streaks are aligned in a direction almost perpendicular to a contour line and parallel to the direction of the maximum slope and in a same direction of the bright wind streak on the spire streak. Slope wind at nighttime, blowing downhill during nighttime cooling on a slope, can be responsible for the formation of the spire streak. This is because the directions of bright wind streaks suggest the upstream side of wind is uphill side of the slope region, the directions of the spire streaks are consistent with the directions of typical direction of the slope wind at nighttime. The initiation point of the spire streak (The higher position of the slope) is upstream side of the wind. Therefore, the directions of spire streaks (and wind streaks) can be used as an indicator of the direction of wind at near surface region on Tharsis volcanoes as we can see in Figure 34.

Table 4: Height and Flank Slopes at Dark Halo

| Volcano                               | Olympus | Ascraeus | Pavonis | Arsia |
|---------------------------------------|---------|----------|---------|-------|
| Height of upper rim of dark halo [km] | 15-21   | 15-18    | 12-14   | 16-18 |
| Height of lower rim of dark halo [km] | 9-15    | 9-14     | 9-12    | 12-17 |
| Flank slope [deg]                     | 5.2     | 7.4      | 4.3     | 5.1   |

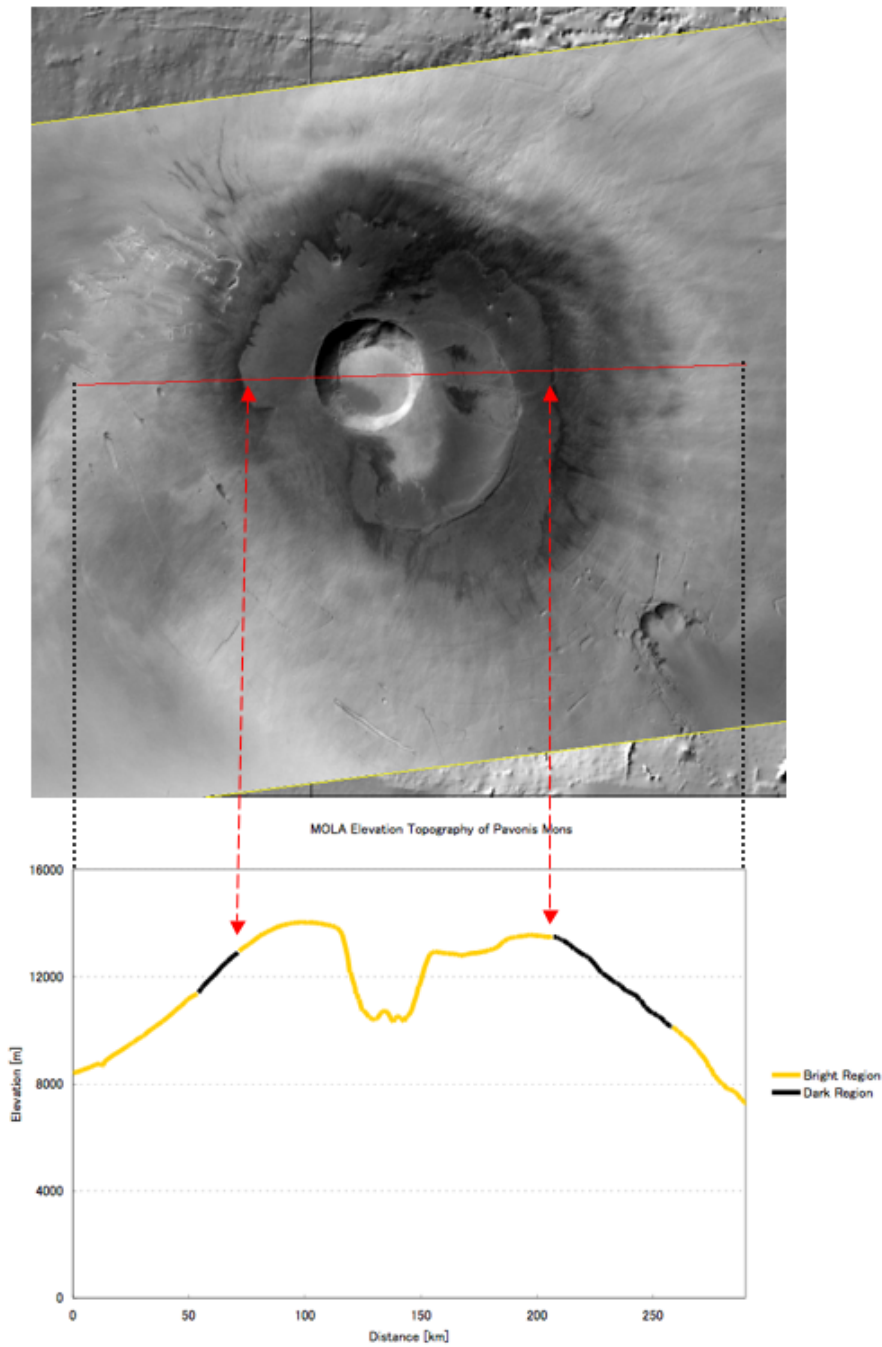


Figure 21: Elevation topography of Pavonis Mons (North-South profile: left side of this figure is the south). Mission Experiment Gridded Data Records (MEGDRs) of Mars Orbiter Laser Altimeter (MOLA) are used to derive this figure. Zero elevation corresponds to the geoid, the equipotential surface corresponding to a distance of 3396 km from the center of mass at the equator. Black and orange lines indicate dark and bright region respectively.

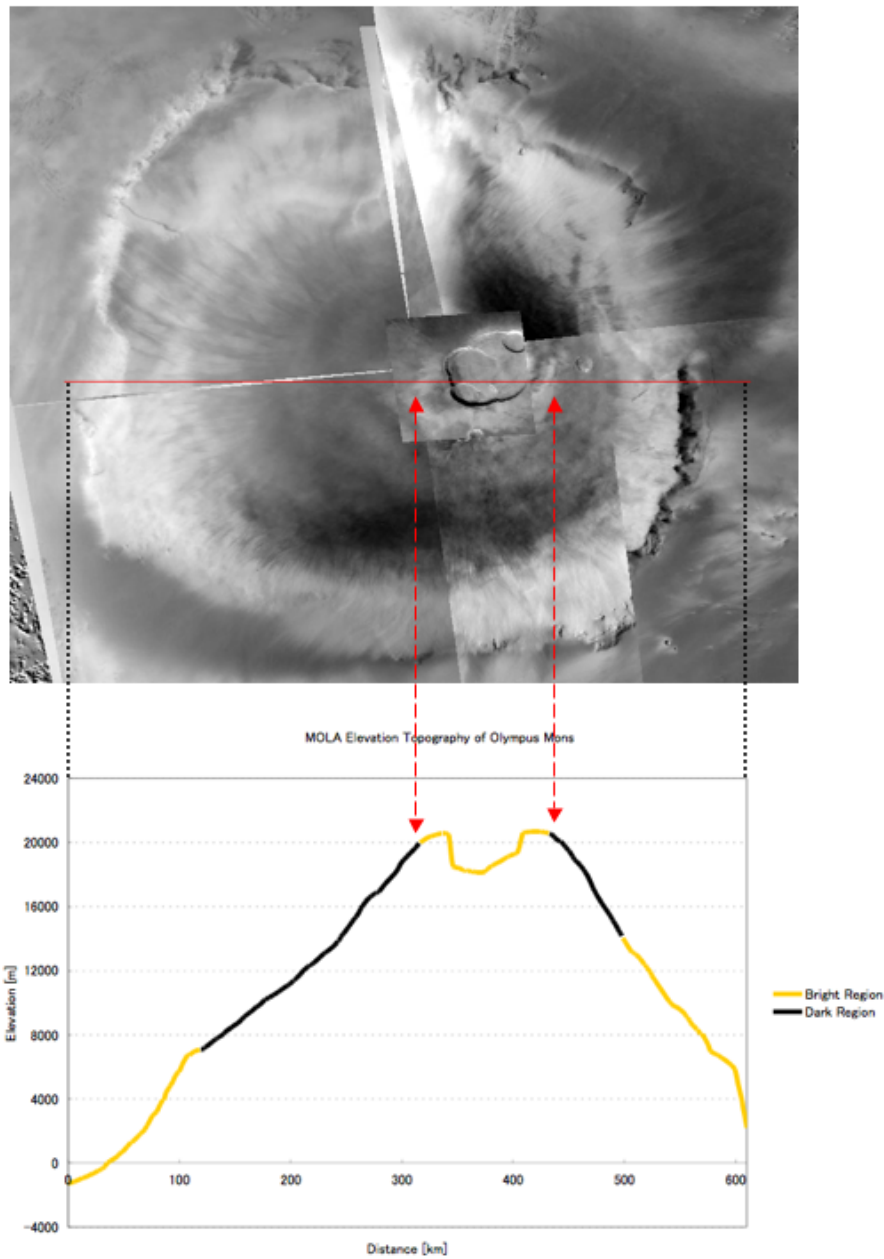


Figure 22: Elevation topography of Olympus Mons (West-East profile: left side of this figure is the west). Mission Experiment Gridded Data Records (MEGDRs) of Mars Orbiter Laser Altimeter (MOLA) are used to derive this figure. Zero elevation corresponds to the geoid, the equipotential surface corresponding to a distance of 3396 km from the center of mass at the equator. Black and orange lines indicate dark and bright region respectively.

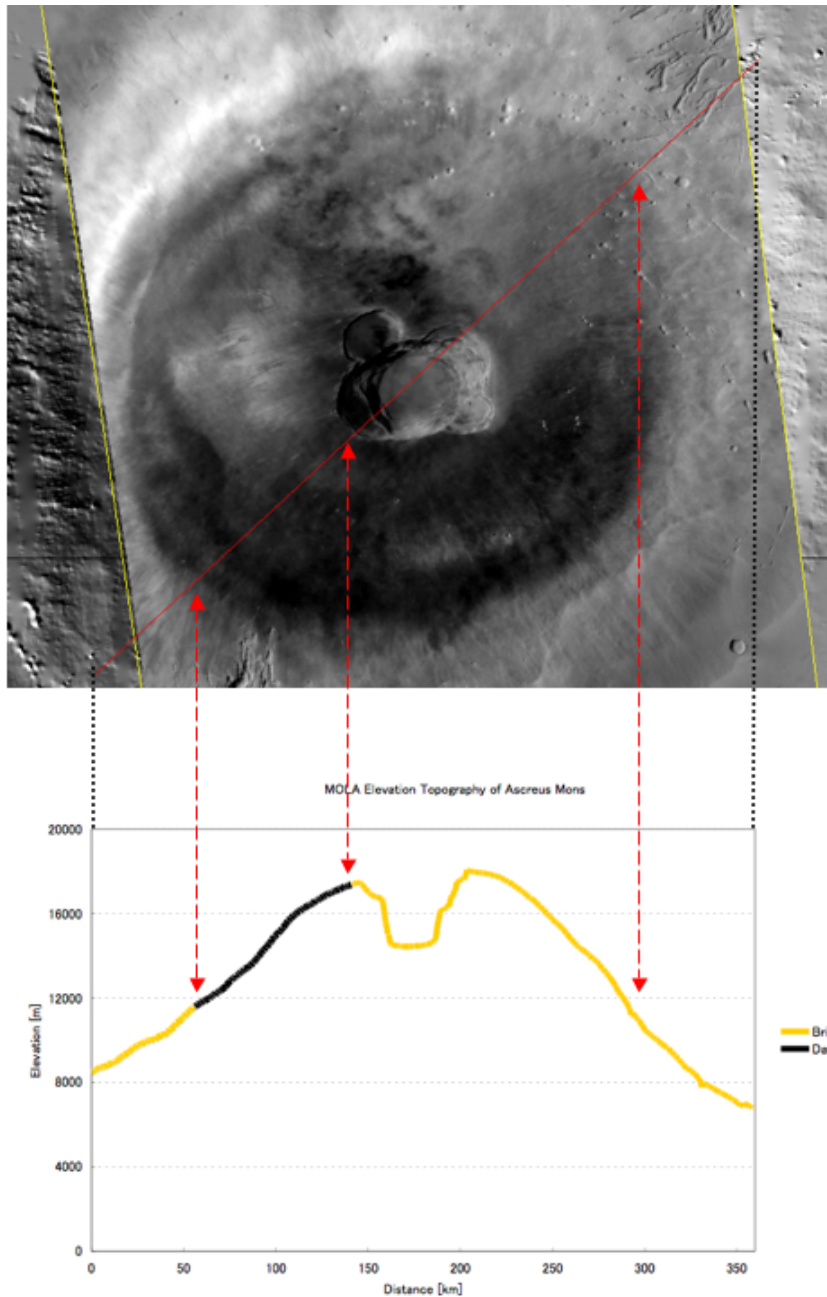


Figure 23: Elevation topography of Ascreus Mons (SW-NE profile: left side of this figure is the SW). Mission Experiment Gridded Data Records (MEGDRs) of Mars Orbiter Laser Altimeter (MOLA) are used to derive this figure. The left side of this figure is the northwest side of the Mons. Zero elevation corresponds to the geoid, the equipotential surface corresponding to a distance of 3396 km from the center of mass at the equator. Black and orange lines indicate dark and bright region respectively.

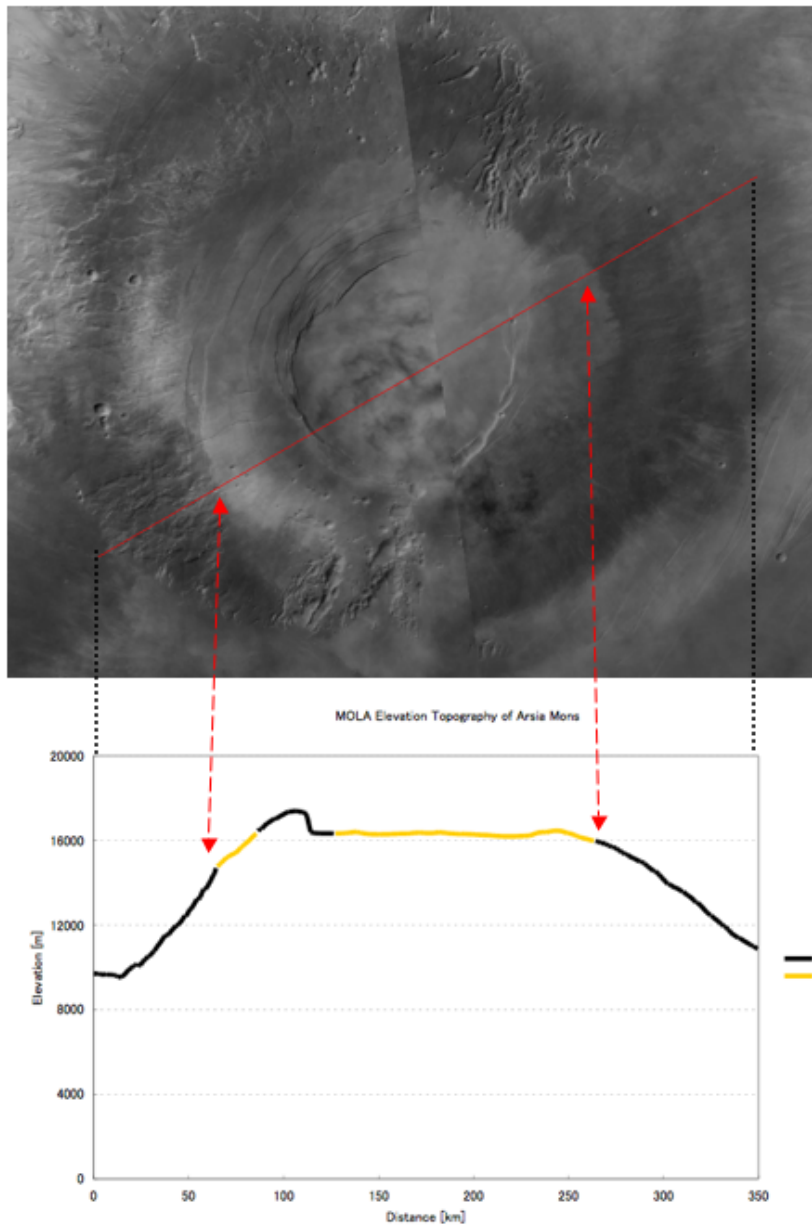


Figure 24: Elevation topography of Arsia Mons. Mission Experiment Gridded Data Records (MEGDRs) of Mars Orbiter Laser Altimeter (MOLA) are used to derive this figure (SW-NE profile: left side of this figure is the SW). The left side of this figure is the east side of the Mons. Zero elevation corresponds to the geoid, the equipotential surface corresponding to a distance of 3396 km from the center of mass at the equator. Black and orange lines indicate dark and bright region respectively.

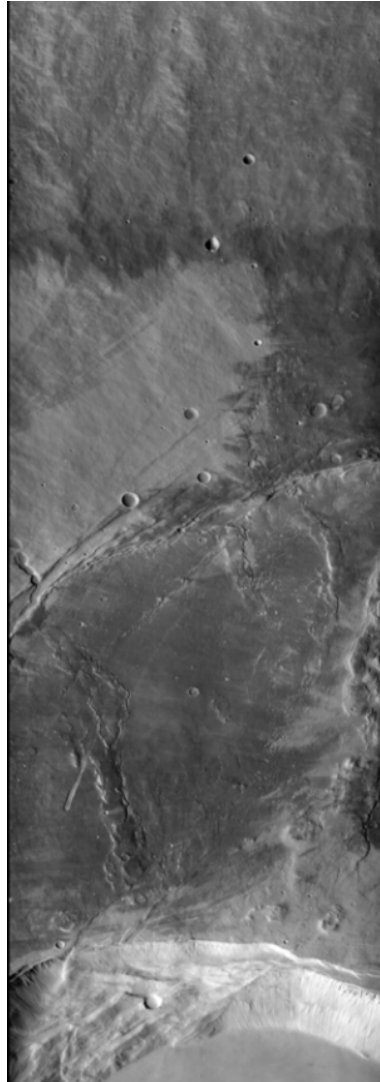


Figure 25: Example of albedo feature in the northern side of the caldera of Pavonis Mons. This image was taken by CTX (P07\_003805\_1805\_XN\_00N112W).

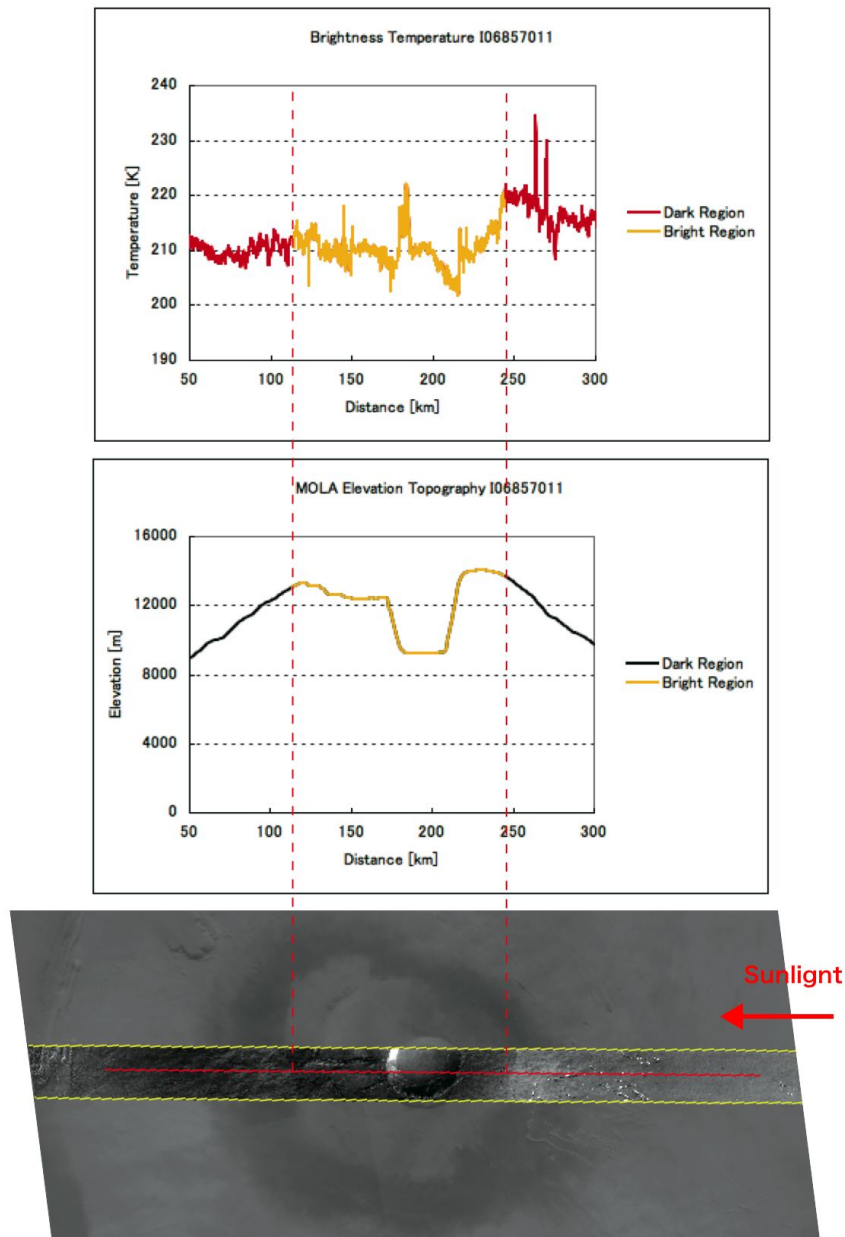


Figure 26: Temperature distribution, elevation topography and daytime IR image of Pavonis Mons. Daytime IR image taken by THEMIS (I06857011) are shown on the MOC global mosaic at the lowest part. The elevation topography from MEGDRs of Pavonis Mons is shown at the middle part. The brightness temperature derived from the IR image (I06857011) is shown at the top.

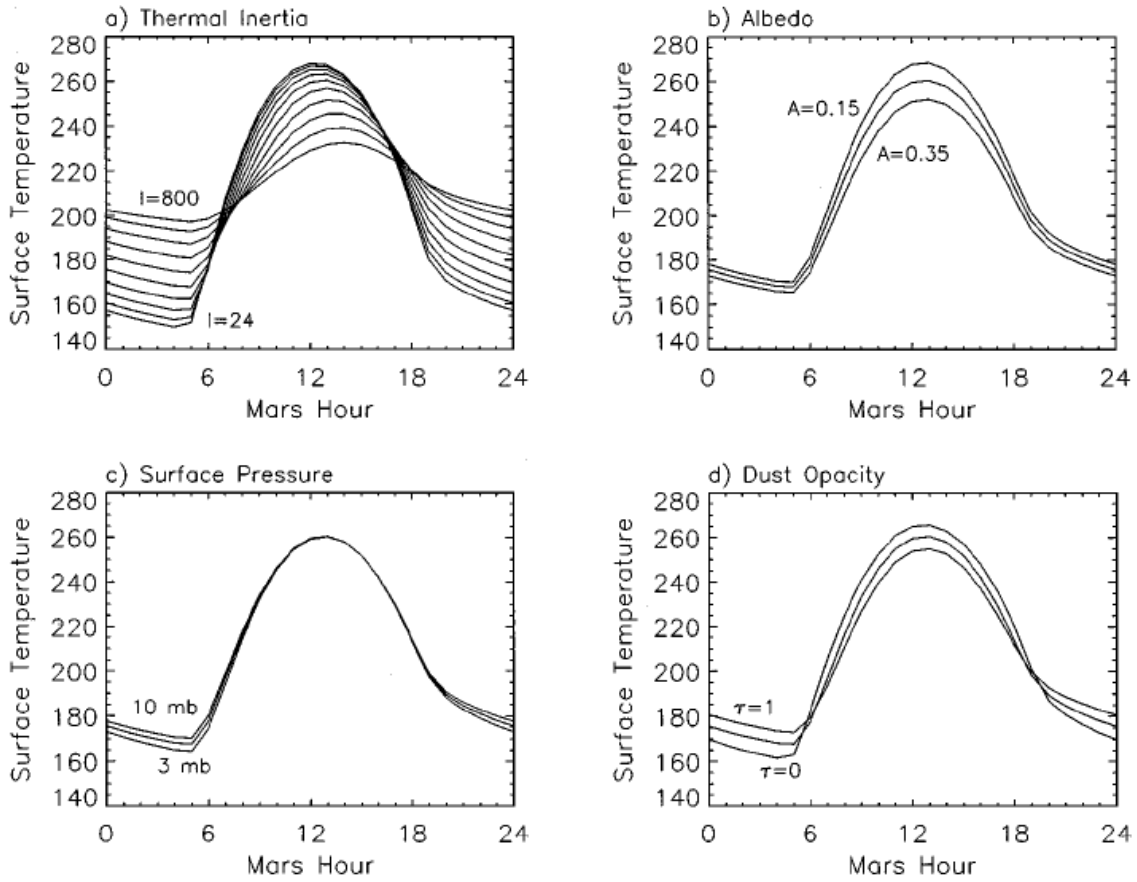


Figure 27: Examples of diurnal variations in surface temperature for different values of independent physical properties used as interpolation nodes in deriving thermal inertia (from Mellon et al., 2000). (a) Thermal inertia. Thermal inertias nodes are 24, 35.43, 52.32, 77.24, 114, 168.4, 248.6, 367, 541.9, and 800 in units of  $\text{Jm}^{-2} \text{K}^{-1}\text{s}^{-\frac{1}{2}}$ . The largest amplitude diurnal temperature cycle corresponds to the lowest thermal inertia and the lowest amplitude cycle corresponds to the highest thermal inertia. (b) Albedo. Albedo nodes are 0.15, 0.25, and 0.35. Lower albedos raise the surface temperatures at all times of day. (c) Pressure. Atmospheric surface pressure nodes are 3, 6, and 10 mb. The lower pressures results in the lower nighttime surface temperatures. Daytime temperatures are minimally effected. (d) Dust opacity. Atmospheric infrared dust opacity nodes are 0, 0.5, and 1.0. Higher dust opacities have the same effect as higher thermal inertias, to reduce the amplitude of the diurnal cycle. All temperatures are given for 50 latitude and an  $L_s$  of 38.8 deg. Invariant parameters in each figure are 114 for fixed thermal inertia, 0.25 for fixed albedo, 6 mb for fixed pressure, and 0.5 for fixed dust opacity.

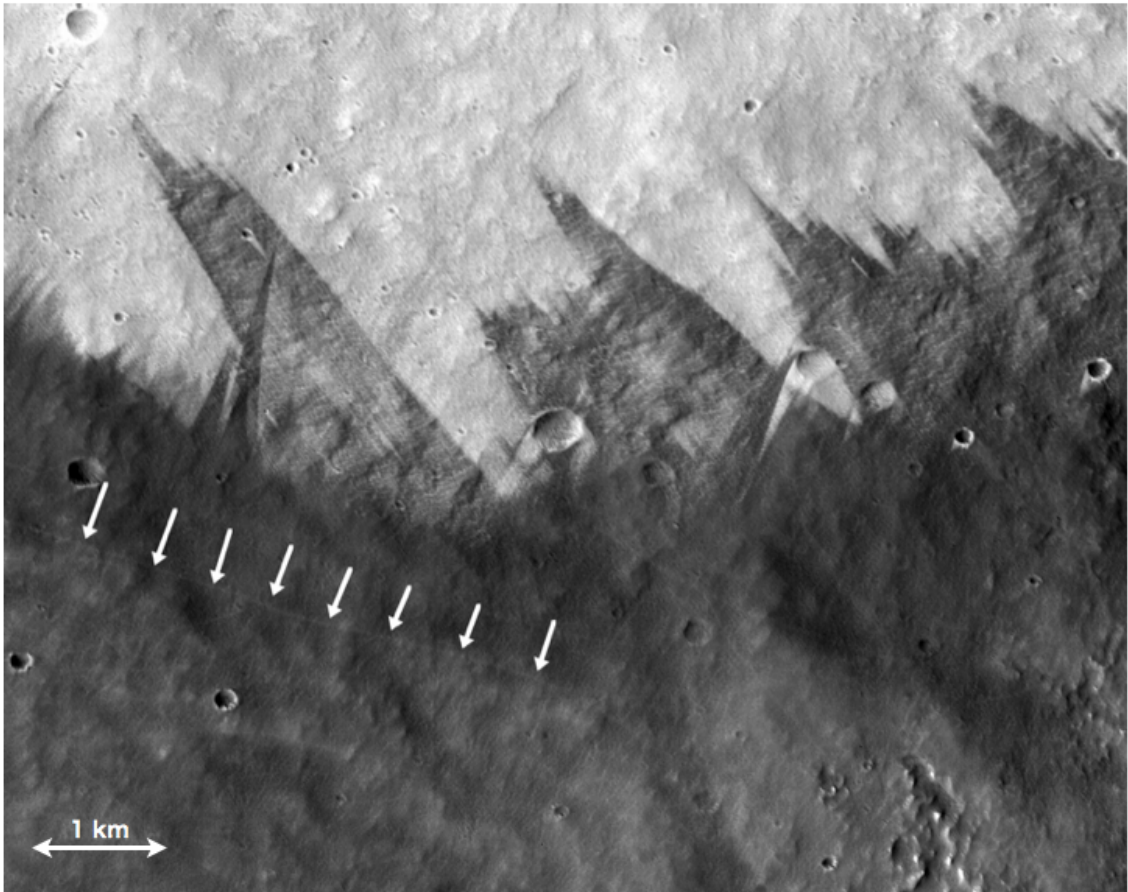


Figure 28: Dust Devil Tracks (DDTs) on the dark halo. This image was taken by Mars Reconnaissance Orbiter (MRO) Context Camera (CTX). Contrast of this image was enhanced to investigate DDTs clearly. A bright track under the white arrows is an example of DDTs. There are many DDTs on the dark halo in this image. We can find "Spire Streaks" that have different directions in this image.

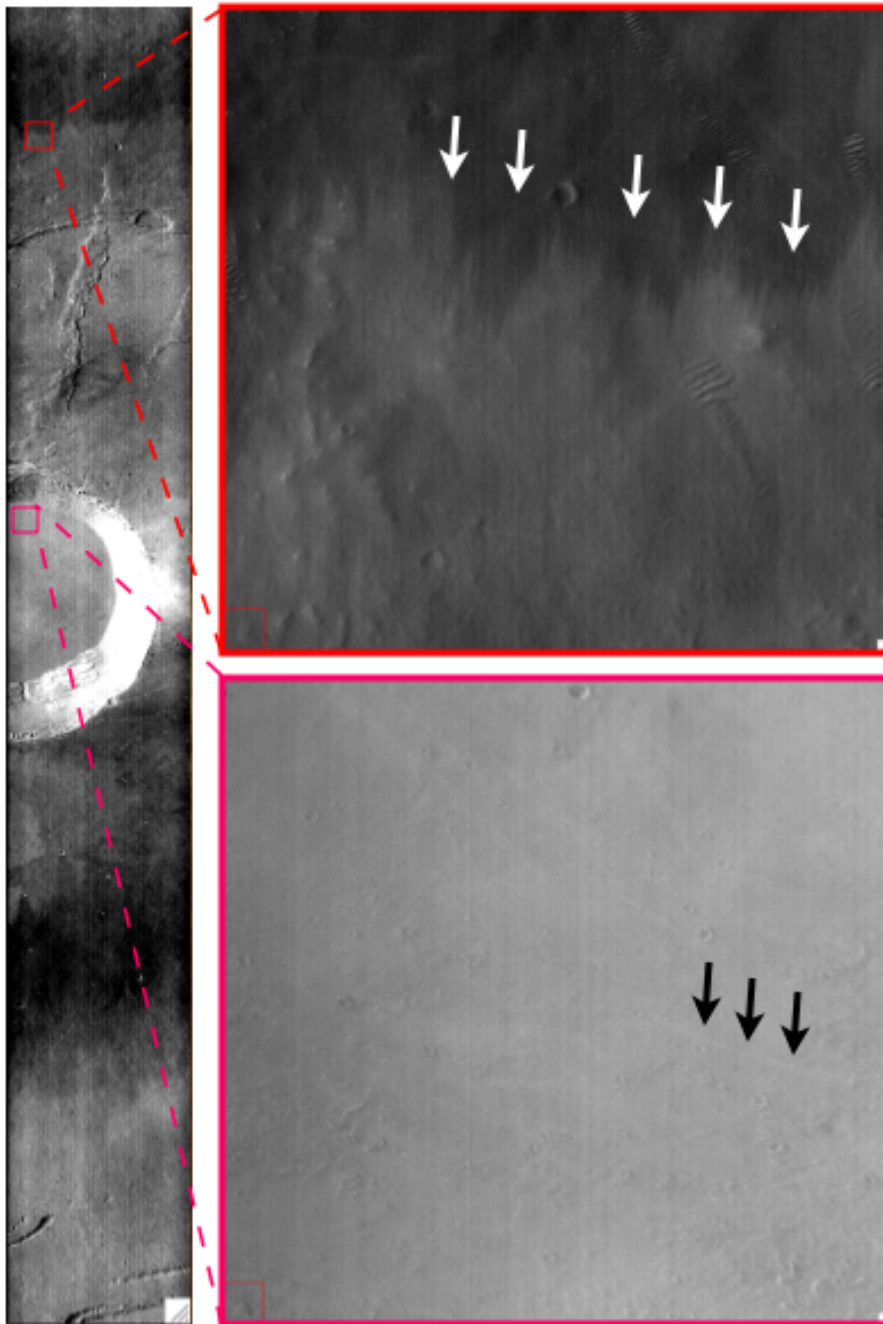


Figure 29: Bright dust devil tracks on dark halo. This image was taken by Mars Reconnaissance Orbiter (MRO) Context Camera (CTX) (P02\_001893\_1804\_XN\_00N113W). Contrast of this image was enhanced to investigate DDTs clearly. Bright tracks under the white and black allows are examples of DDTs.

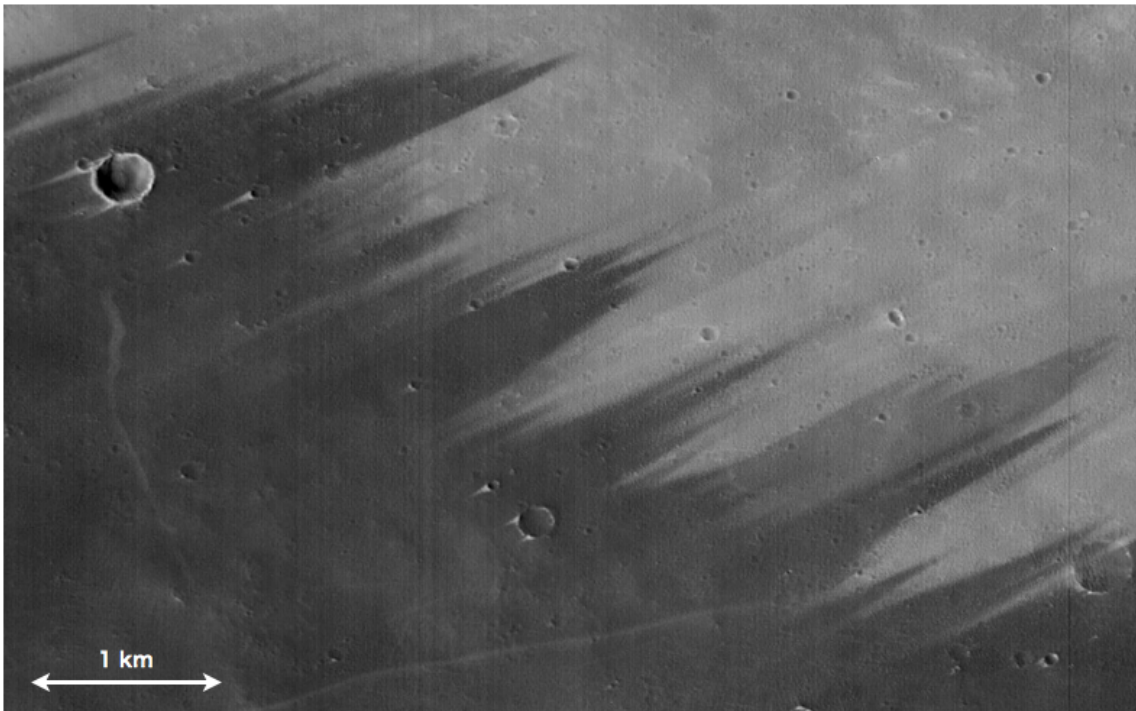


Figure 30: Close-up image of spire streaks (taken by CTX: P08\_004227\_1826\_XI.02N113W). No related obstacle is found at start point of the streak.

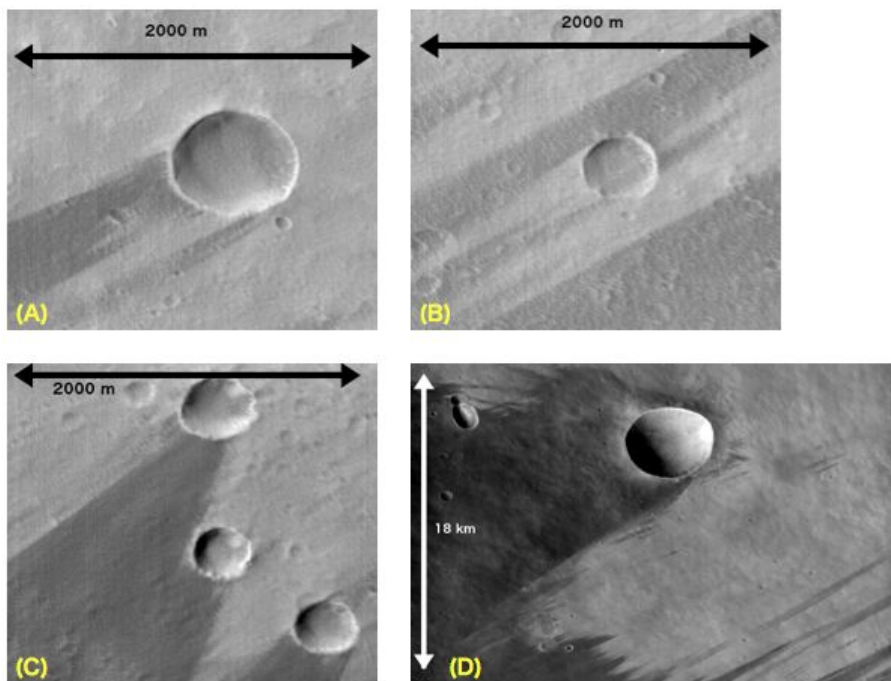


Figure 31: Craters around or on spire streaks taken by MRO CTX.

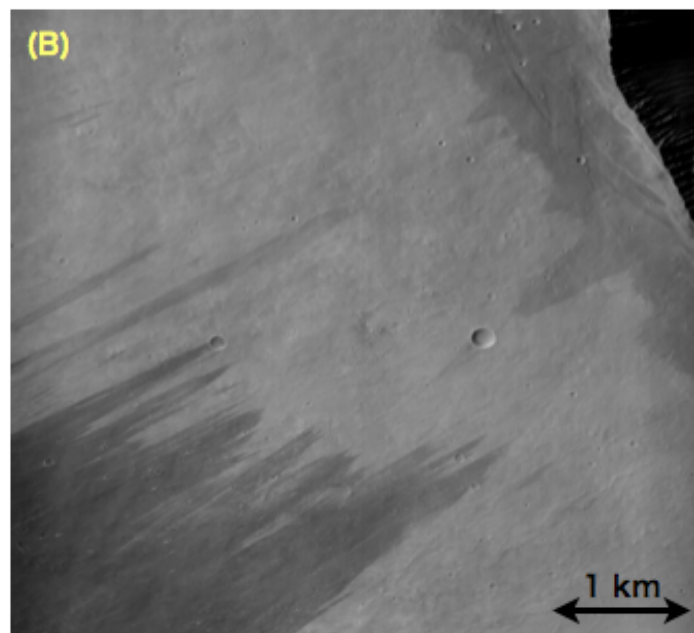
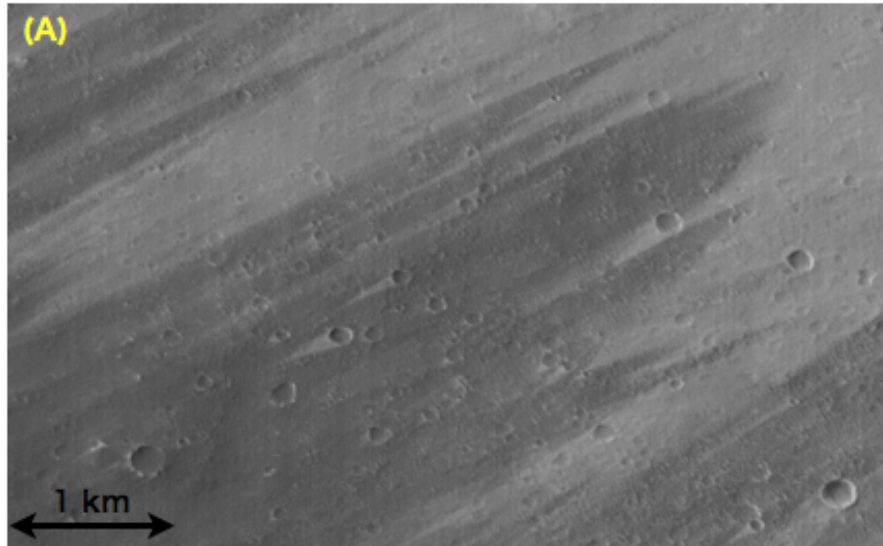


Figure 32: Close-up images of spire streaks taken by MRO CTX. (A) Spire streaks and bright wind streaks in the inner rim of the dark halo. (B) Sharp and dull spire streaks around the rim of caldera.

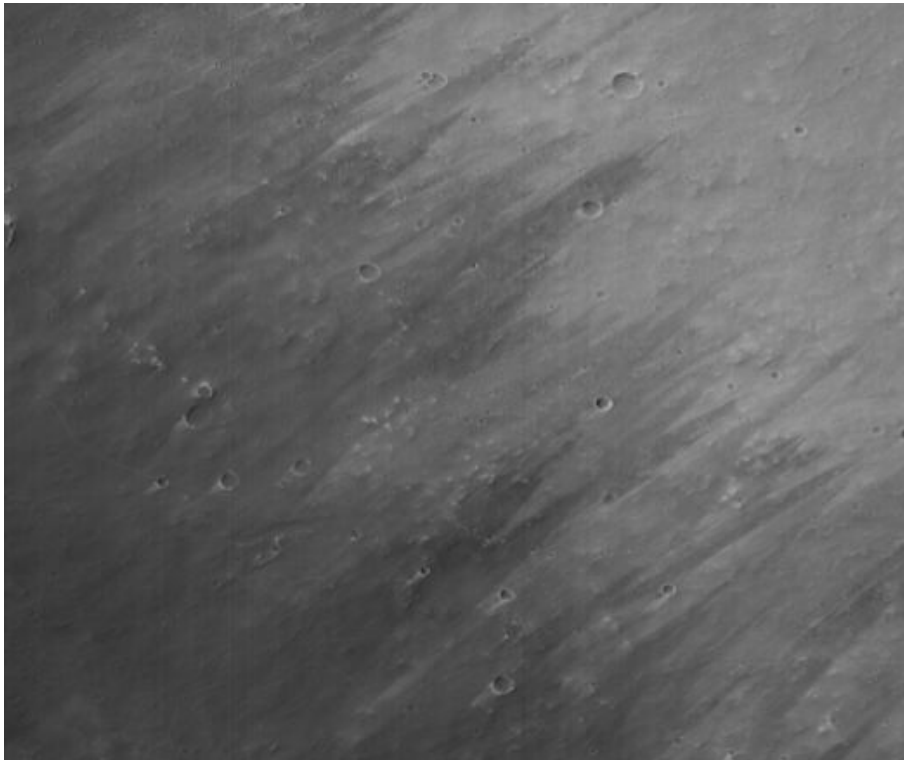


Figure 33: Gradation on the inner rim of the dark halo. This image was taken by MRO CTX

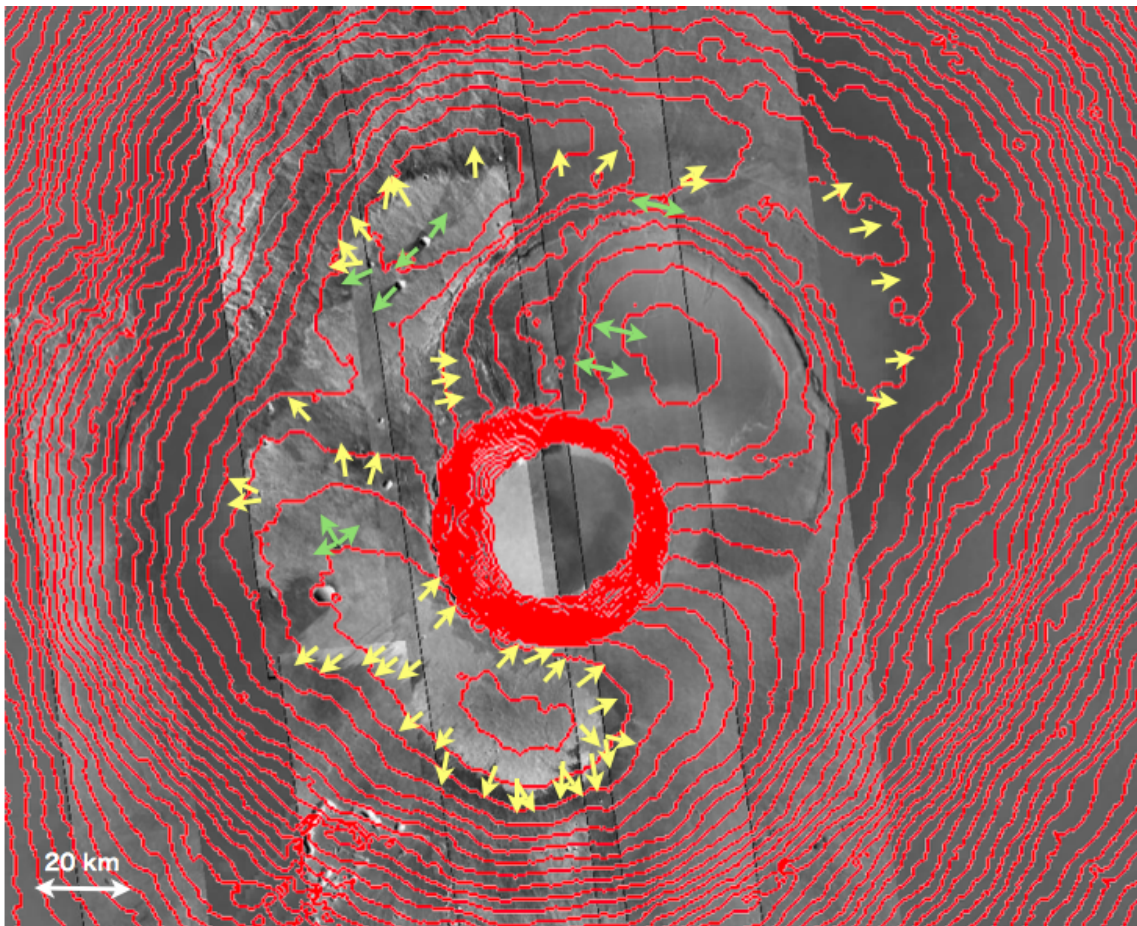


Figure 34: Distribution of spire streaks at Pavonis Mons. Contour lines (by 200 m) are shown on a mosaic image of CTX. Yellow arrows indicate spire streaks, and the root of the arrows are narrow side of spire streaks. Green arrows indicate dark streaks which is probably a kind of eolian streak, and the root of the arrows are the upstream side of estimated wind directions.

### 3.2 Temporal changes in patterns

Repeated imaging by successive spacecrafts for long time provides good data source to evaluate the temporal variation of the dark halo and the spire streak.

In this thesis, pattern changes at southwest region of the caldera (the circle colored orange in Figure 35) and at southeast region of the caldera (the circle colored orange in Figure 36) are investigated. The former region is suitable to investigate time-variable changes of spire streaks because many clear spire streaks are found and show drastic changes in its pattern. The latter region, having less clear spire streaks, is suitable to investigate time-variable changes of brightness of dark halo because the region shows drastic changes in its brightness.

Figure 35 shows a pattern change between 1978 and 1999. However, optics of Viking is different from that of Mars Global Surveyor (MGS) Mars Orbiter Camera (MOC). Therefore, it is hard to say that the pattern which was not found in the Viking image has emerged in the MOC image.

Figure 36 shows a pattern change from 2001 to 2003 (one Martian year). All images in Figure 36 are taken by MGS MOC. A global dust storm (GDS) has occurred in 2001 [Cantor, 2007]. GDS 2001 has occurred at the timing between E0501238 and E0900848 in Figure 36. GDS 2001 began near Hellas just before southern spring equinox ( $L_s = 177$  deg) [Strausberg et al., 2005]. As the dust storm reached the western edge of Tharsis, secondary dust lifting centers developed in southeastern region of Tharsis. Subsequently, the storm rapidly encompassed the planet (by  $L_s = 193$  deg). GDS 2001 is estimated to terminate active lifting of dust at between  $L_s = 210$  deg and  $L_s = 214$  deg. Although not all changes are related to Global Dust Storm (GDS), it seems that GDS causes major changes in the pattern of the dark halo. The upper boundary of the dark halo at SW side moved to lower area and changed its shape after GDS 2001 (Figure 36). The dark albedo feature at the SE side of the caldera (surrounded by the orange circle in Figure 36) has disappeared once after GDS 2001 (E0900848 in Figure 36) and seems to re-appear as time goes on. Sedimentation of fine dust should be responsible for erasing the pattern.

Spire streaks in the southwest region of the caldera was re-formed after GDS 2001 (arrow colored pink in Figure 36), and brightness of the northeast region of the caldera also changed (circle colored orange in Figure 36). Phase angle. of the images are not corrected, and span 31.96–50.16 deg. However, changes mentioned above are observed regardless of the phase angles. In other words, differences of phase angles between each

images is not responsible for the temporal changes of the dark halo.

Figure 37 also shows a pattern change taken by MGS MOC. Linear streaks that were not found in R1400388 appeared in S0802608. Not all linear streaks are spindle-shaped like spire streaks.

Figure 38 shows brightness ratio of bright and dark region on the dark halo. Brightness ratio of Figure 38 is the ratio of brightness of concerned region to that of caldera floor whose brightness shows no apparent correlation with local time and season in MOC images.

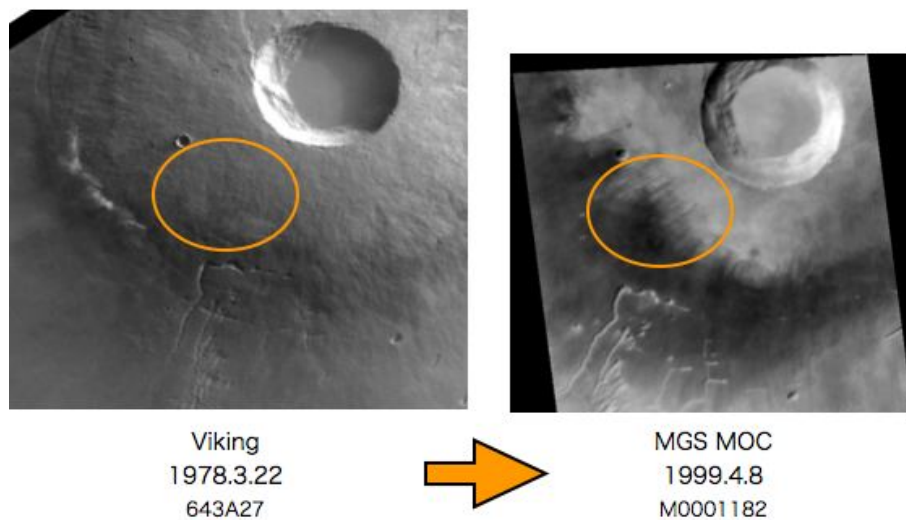


Figure 35: Temporal changes of the dark halo from 1978 to 1999. Left image was taken by Viking orbiter (643A27), and right image was taken by MGS MOC (M0001182).

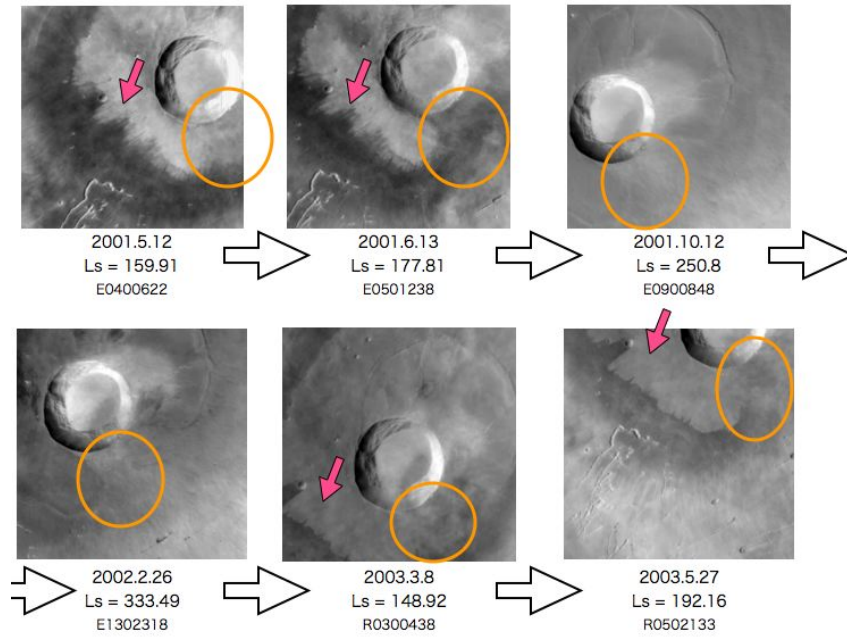


Figure 36: Temporal changes of the dark halo from May 2001 to May 2003. All images are taken by MGS MOC.

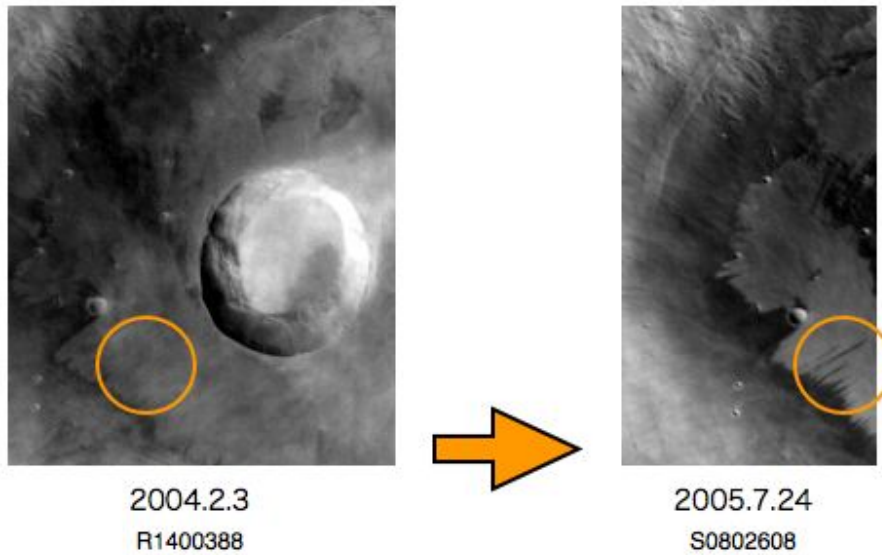


Figure 37: Temporal changes of the dark halo from 2004 to 2005. Both images are taken by MGS MOC.

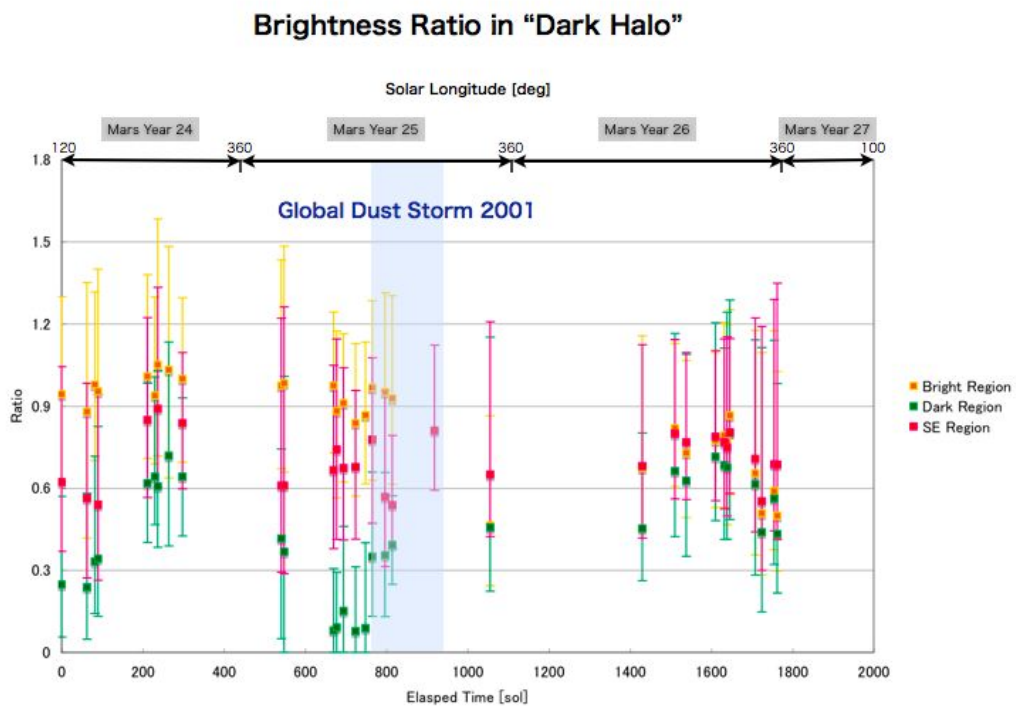


Figure 38: Brightness ratio between bright region and dark region in the dark halo. Brightness ratio is the ratio of brightness of concerned region to that of caldera floor. The ratio was derived from MGS MOC images.

## 4 Discussion

### 4.1 Possible origins of the spire streak derived from the morphology

There are only two possible origins of dark albedo feature such as spire streak: 1) erosional origin: removal of fine dust by strong wind, and 2) depositional origin: deposition of wind-blown material (dark material or coarser grained particles).

A topographic obstacle at the upstream region is needed to make a spindle-shaped feature on the surface. In erosional process to make wind streaks, strong turbulence of the air occurs at the lee of a topographic obstacle. It is quite unlikely for such turbulence to begin with a point like region ( $<$  a few meters). Furthermore, such turbulence hardly get wider with increasing distance because such turbulence at the lee of a obstacle weakens with increasing distance. Therefore, a spindle-shaped feature can be formed only if particulate materials are supplied into the atmosphere as a plume and deposit on the surface (Figure 39). Whether the "initiation point" of a spire streak is leeward side is critical information to know the formation process of a spire streak.

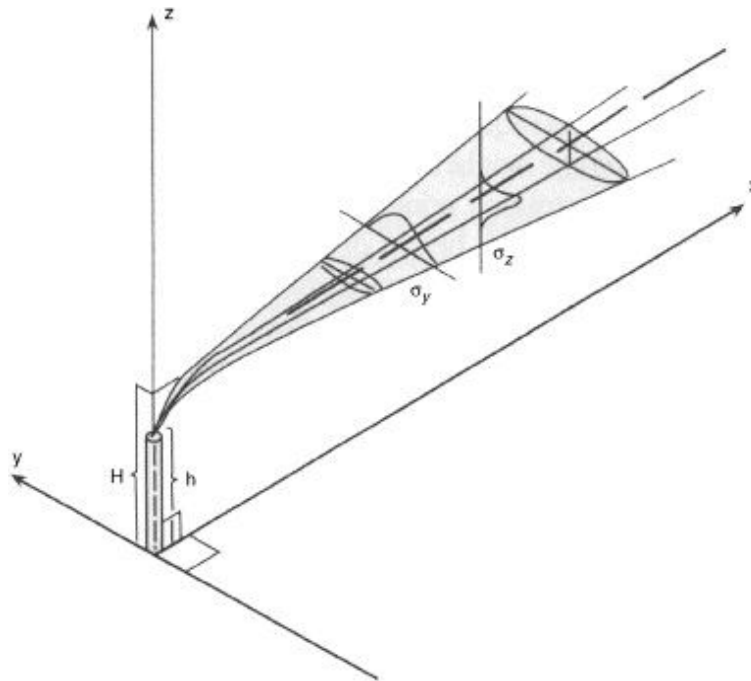


Figure 39: Wind-blown plume source.

As mentioned in the previous section, the initiation point of a spire streak is usually at the upstream side of wind. Therefore, depositional origin is suggested from interactions between spire streaks and slope wind at nighttime. The global wind around Pavonis Mons

is mostly in the west through all seasons, and the global surface wind directions are little affected by orbital parameter or dust-loading variations within ranges that appear applicable to the recent geological past (last few million years at least) [Fenton and Richardson, 2001]. Fenton and Richardson also said that wind speeds are affected by changes in orbital parameters and dust-loading variations. The nighttime slope wind seems to be more important than the global wind for the formation of the spire streaks because the directions of the spire streaks are mostly consistent with that of nighttime slope wind as seen in Figure 34. However, the global wind might get stronger and affect the direction of the spire streaks under some rare circumstances. The spire streaks that have different directions at same place (seen in Figure 34) might reflect variations of the global wind and local slope wind.

Other features of spire streaks are also consistent with depositional origin. Wind-blown material can pass over topographic obstacles. Bright DDTs on spire streaks can be explained as removal of dark material by a dust devil. In short, a depositional origin is favored from the morphological evidences. However, we still don't know the origin of the source of depositional materials.

The depositional materials must be responsible for the dark albedo feature. Basaltic sand [Geissler et al., 2008] and scoria come from mafic volcanism are common as dark materials. However, it is not a natural story that solid material such as sand or scoria emanated from a point like region. It is more likely for some kind of volatiles to emanate from the sub-surface. Can water, carbon dioxide and sand be the emanating material? In following sub-sections, I will discuss the possibility of them as emanating materials.

## 4.2 Material that cause temporal changes in patterns

Sedimentation of fine dust should be responsible for erasing the pattern. Formation of spire streak doesn't seem to be continually lasting phenomena. Major changes were found only at four times from 1978 to 2007. Irregular wind velocity on the surface supposed to control formation of spire streak. The streaks that have different directions at same place (Figure 46) are consistent with such a mechanism.

Seasonal changes of brightness might be found in the dark halo if its dark appearance is due to deposition of volatiles. Between before and after global dust storm (GDS) 2001, the absolute brightness of the inner bright region of the dark halo seems to be changed (Figure 38). Probably this is because fine dust deposited on the summit of Pavonis Mons during GDS 2001. However, brightness of "inner bright region" and "south-east region from the direction of caldera floor" doesn't show seasonal changes (Figure 38). On the other hand, brightness of the dark halo quickly changes, though we cannot define whether the changes are related to Martian seasons or not (Figure 38). There seems to be no apparent relation between temporal change of the dark halo and any kind of volatiles.

## 4.3 Possibility of the phase change phenomena at the dark halo

Since the appearance of the dark halo is so distinct and regular, this may suggest the formation of the dark halo is deeply associated with the phase change phenomena. Plausible phase change is gas-solid transition of  $\text{CO}_2$  and  $\text{H}_2\text{O}$ . If the surface/subsurface environment changes and it induces the phase change, distinct change in the surface pattern and the albedo may arise. To evaluate this possibility, we estimate (P, T) conditions at and around the dark halo.

Figure 40 and 41 shows seasonal and daily variations of the surface pressure on the Mars Exploration Rovers (MERs) landing sites. R. M. Haberle and R. J. Wilson estimated surface pressure as a function of  $L_s$  and local time for the two rover sites with numerical modeling of martian atmosphere [Smith et al., 2006]. They obtained an equation for Spirit as

$$\begin{aligned} p_{surf}(L_s, t) = & 6.917 + 0.342 \cos[L_s - 333] + 0.377 \cos[2(L_s - 75)] \\ & + 0.076 \cos[3(L_s - 11)] + 0.044 \cos[4(L_s - 68)] \\ & + 0.189 \cos[360(t/24 - 0.26)] \\ & + 0.057 \cos[720(t/24 - 0.40)] \text{ mbar} \quad (1) \end{aligned}$$

and Opportunity as

$$\begin{aligned}
 p_{surf}(L_s, t) = & 6.682 + 0.355 \cos[L_s - 340] + 0.430 \cos[2(L_s - 76)] \\
 & + 0.079 \cos[3(L_s - 12)] + 0.047 \cos[4(L_s - 68)] \\
 & + 0.193 \cos[360(t/24 - 0.26)] \\
 & + 0.059 \cos[720(t/24 - 0.41)] \text{ mbar} \quad (2)
 \end{aligned}$$

where  $t$  is local time measured in hours, with 24 hours in a sol. In this thesis, these functions and Digital Elevation Model (DEM) of Mars are used to estimate the surface pressure at the place of the dark halo.

We can estimate the surface pressure  $P$  using

$$P = P_0 \exp\left(-\frac{z}{H_s}\right) \quad (3)$$

where  $P_0$  is standard pressure given by equation (1) or (2),  $H_s$  is scale height (12 km in standard climate model of Mars) and  $z$  is the difference of height between the point that we concern and the landing sites of Spirit and Opportunity.

Seasonal changes of brightness temperature were obtained from data of THEMIS. Daytime temperatures at the dark halo and its surroundings are estimated for the daytime image of THEMIS-IR (taken mostly at 15:00 – 18:00 local time). Figure 42 shows the seasonal variation of the temperatures at the dark region (in side the dark halo) and the surrounding bright region. The nighttime temperatures are also estimated for the nighttime image of THEMIS-IR (taken mostly at 3:00 – 6:00 local time) (43). The temperature difference between the dark region and the bright region is mostly less than 10 K and the typical value would be several to 10 K. Figure 44 shows the seasonal variation. This seems to have a maximum value around  $L_s = 270$ . There is almost no temperature difference between the dark and the bright region in nighttime throughout the Martian year. The contrasting feature in the difference of temperature between daytime and nighttime suggest this difference is not caused by the difference of thermal inertia (hence, the difference in the grain size) between the dark halo and the surrounding bright region, but it is due to the difference in albedo.

Figure 45 shows a phase diagram on the surface of Pavonis Mons. Daytime temperature of the dark halo is always above the condensation temperature of carbon dioxide. Nighttime temperature of the dark halo is near the condensation temperature of carbon dioxide. We cannot directly refer the phase change of water without the information of partial pressure of water.

Phase difference of carbon dioxide doesn't seem to be responsible for formation of the dark halo. There is no apparent phase difference between dark region on the dark halo and inner bright region of the dark halo (Figure 45). Phase of water on Pavonis Mons cannot be known because we don't have information on partial pressure of water. Solid water exists under the surface, and liquid water could occur transiently near the surface today under certain conditions on Mars. However, deposition of water ice seems to make albedo larger.

The dark halo and its surrounding region are under similar environment in pressure and temperature. The temperatures showed in 45 don't cover the all range of daily temperature because IR images are only snapshots. Besides, (P, T) varies according to location, and subsurface pressure easily changes according to whether the region is connected to the surface above. Therefore, CO<sub>2</sub> at the dark halo might be able to change its phase under extraordinary circumstances because the (P, T) at nighttime is around the phase boundary (Figure 45). As mentioned in the previous section, spire streak are also formed under extraordinary circumstances. The relationship between the phase of CO<sub>2</sub> and the spire streak have to be more closely investigated in future works.

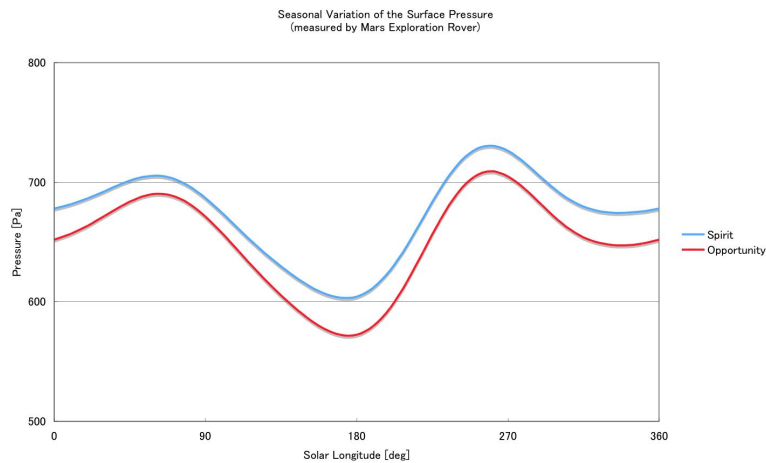


Figure 40: Seasonal variation of the surface pressure measured by Mars Exploration Rover [Smith et al., 2006]. The pressure was derived by substituting  $t = 15$  into the equation (1) and (2).

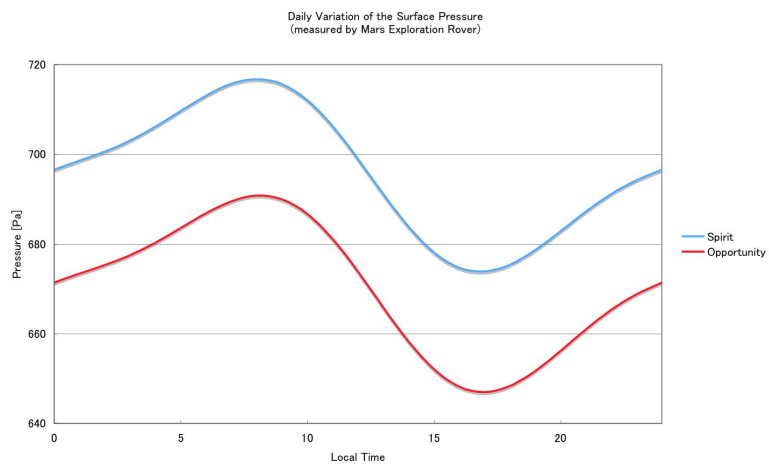


Figure 41: Daily variation of the surface pressure measured by Mars Exploration Rover [Smith et al., 2006]. The pressure was derived by substituting  $L_s = 0$  into the equation (1) and (2).

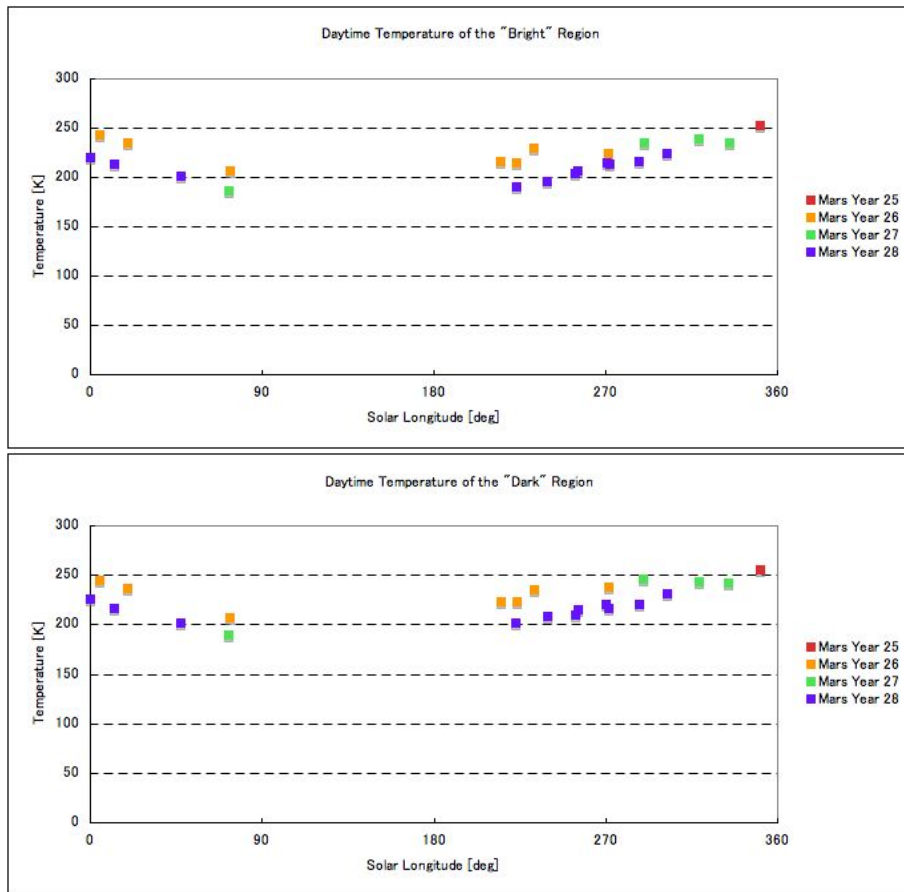


Figure 42: Daytime temperature on the dark halo. Above) seasonal changes of daytime temperature on "Bright Region". Below) seasonal changes of daytime temperature on "Dark Region". Errors are small enough to ignore. Temperature was derived from THEMIS IR images (of Mars Odyssey) from 2002.3.31 (Mars Year 25) to 2007.12.14 (Mars Year 29).

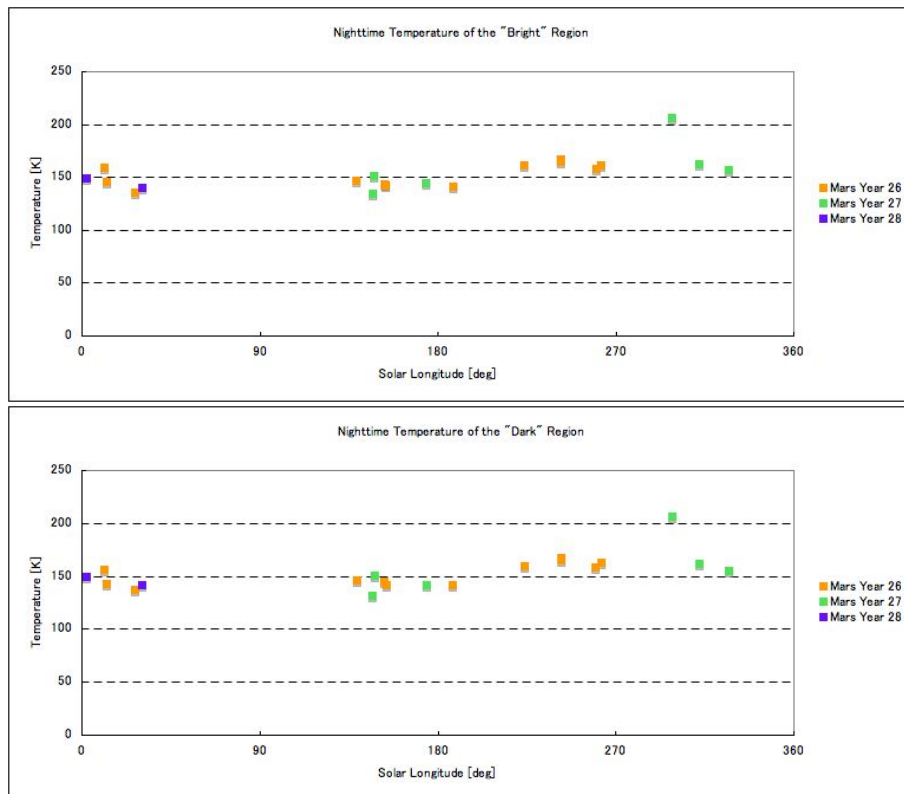


Figure 43: Nighttime temperature on the dark halo. Above) seasonal change of nighttime temperature on "Bright Region". Below) seasonal changes of nighttime temperature on "Dark Region". Errors are small enough to ignore. Temperature was derived from THEMIS IR images (of Mars Odyssey) from 2002.3.31 (Mars Year 25) to 2007.12.14 (Mars Year 29).

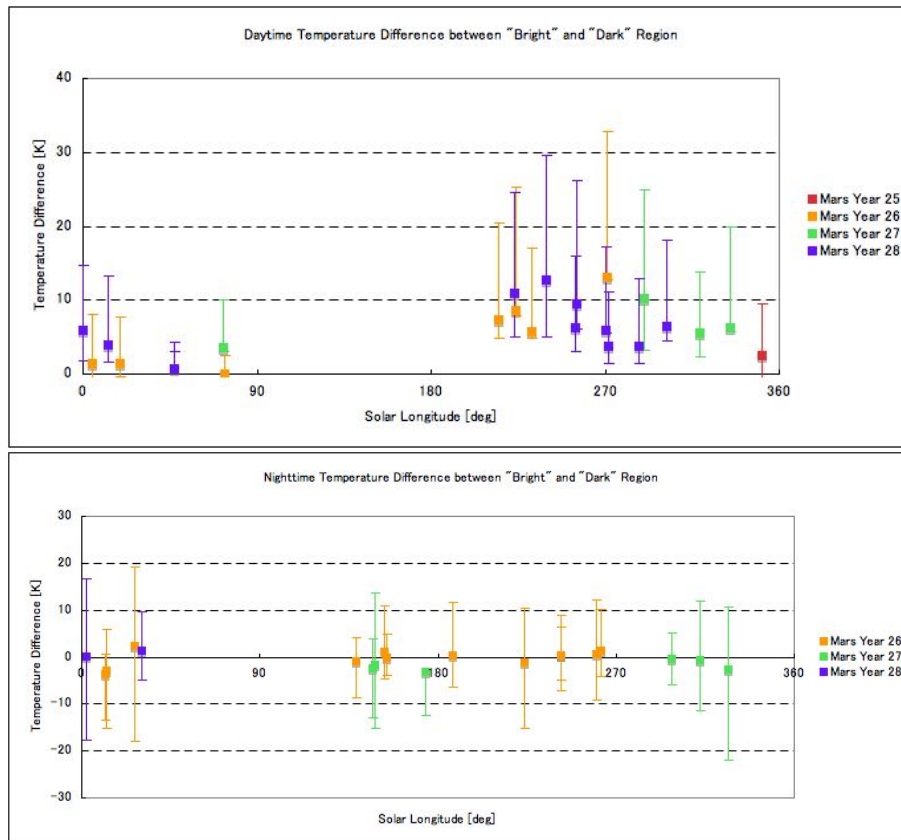


Figure 44: Seasonal changes of temperature difference between bright and dark region. Temperature was derived from THEMIS IR images (of Mars Odyssey) from 2002.3.31 (Mars Year 25) to 2007.12.14 (Mars Year 29).

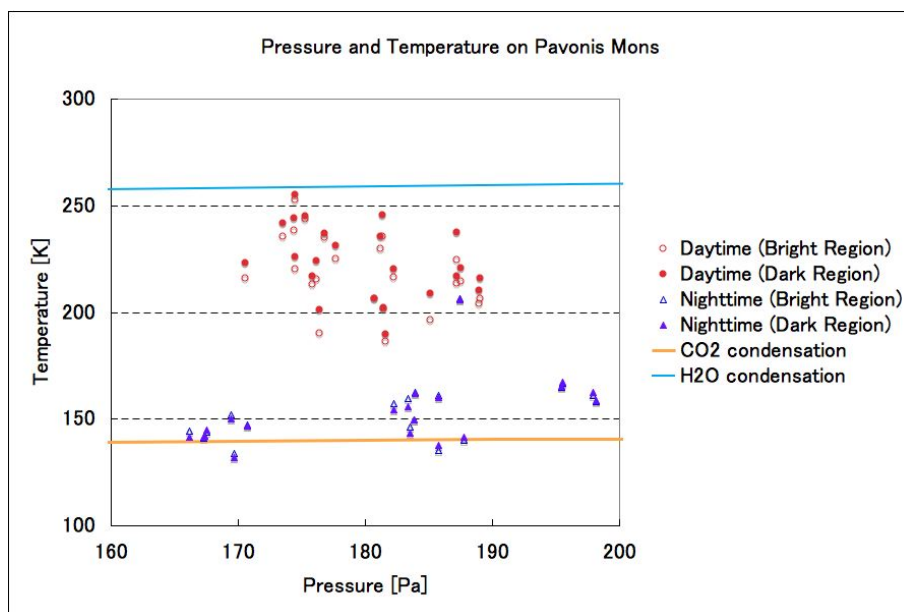


Figure 45: Phase diagram on the surface of Pavonis Mons. Temperature was derived from THEMIS IR images (of Mars Odyssey) from 2002.3.31 (Mars Year 25) to 2007.12.14 (Mars Year 29). Pressure was estimated from equation (1) and equation (3).

#### 4.4 Cause for albedo difference

Amount of dust seems to be responsible for albedo difference. Dust Cover Index (DCI) that was developed by [Ruff and Christensen, 2002] shows that Pavonis Mons is highly dust-covered (Figure 46 Middle). Inner bright region of dark halo is especially rich in silicate dust. The dark halo is lower dust-covered compared to the inner bright region.

Low value of thermal inertia on Pavonis Mons is consistent with highly dust-covered surface [Putzig et al., 2005]. Both bright and dark region on Pavonis Mons has low value of thermal inertia (below  $100 J/m^2 K s^{1/2}$ ). No difference is found in thermal inertia between dark and bright region of Pavonis Mons (Figure 46 Below). This means that a thin ( $<$  several mm) layer controls the albedo difference. Deposition/erosion of thin layer of dust can control the albedo difference.

Erosional origin is suggested if albedo difference is caused by dust. Removal of fine dust by strong wind is more natural story to make albedo dark than deposition of coarse-grained particle. We cannot find the source of coarse-grained particles that can form the spire streak.

Other dark material could have deposited and formed spire streaks. In this case, some kind of volatiles must be responsible for the albedo difference because It can hardly be expected for solid materials to emerge from underground. Volatiles that emerged in the form of gas might change their form to solid and deposit on the surface.

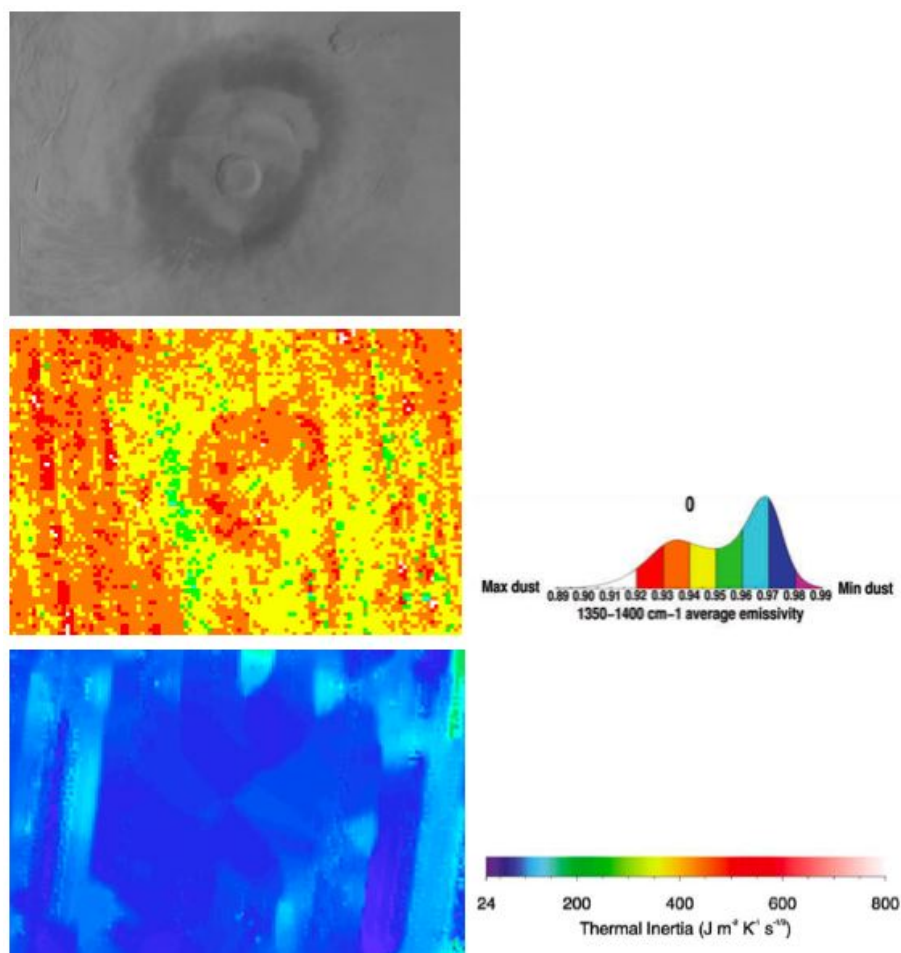


Figure 46: Dust Cover Index (DCI) and thermal inertia of Pavonis Mons. Above) mosaic image of Pavonis Mons taken by Mars Orbiter Camera (MOC) of Mars Global Surveyor (MGS). Middle) DCI obtained by [Ruff and Christense, 2002]. Below) thermal inertia obtained by [Putzig et al., 2005].

## 5 Conclusion

The author proposes two possible origins of the spire streaks: 1) erosion of fine dust by gusty strong slope wind, and 2) deposition of wind-blown volatiles. Both origins are consistent with that albedo of those regions are controlled by thin layer on the surface. Table 5 is a "Score Sheet" of each theory for formation of the dark halo.

1) If erosional process actually works, spire streak indicates completely a new kind of wind-surface interaction that can make spindle-like shape. Erosional process can be consistent with dark features on the slope of Pavonis Mons and high value of Dust Cove Index (DCI), though it isn't consistent with the shape of spire streaks, streaks crossing over obstacles and bright dust devil tracks at the dark halo.

2) If depositional process actually works, spire streak indicates emerging materials that haven't discovered ever. Depositional process can be consistent with the shape of spire streaks and streaks crossing over obstacles and bright dust devil tracks at the dark halo, though it isn't consistent with dark features on entire slope. Furthermore, we don't know possible material that can emerge from under the current Martian surface.

Table 5: "Score Sheet" of each theory for formation of the spire streak

|                              | 1) Erosion of fine dust | 2) Deposition of Volatiles |
|------------------------------|-------------------------|----------------------------|
| Shape of "Spire Streak"      | NO                      | OK                         |
| Crossing over obstacles      | NO                      | OK                         |
| Bright dust devil tracks     | NO                      | OK                         |
| Cause for albedo difference  | OK                      | NO                         |
| Difference of DCI            | OK                      | NO                         |
| Low value of thermal inertia | OK                      | OK                         |

## 6 Summary and Future Work

Data from visible imagers, imaging spectrometers, laser altimeter and numerical modeling are investigated to understand the formation process of the spire streaks and the dark halo.

The author proposes two possible origins of the spire streak: 1) erosion of fine dust by gusty strong slope wind, and 2) deposition of wind-blown volatiles. Both origins are completely new kind of wind-surface interactions that haven't ever discovered.

Future work will contain analysis of spectral data that was produced by recent high-resolution instruments to know the difference of surface material between the dark halo and its surrounding region.

## Acknowledgements

The author wishes to express his sincere appreciation to Professor Kei Kurita of the Earthquake Research Institute for his guidance during master's course and for stimulating discussions. The author would like to thank Dr. I. Yoshikawa of the University of Tokyo for his introductory training during first year of master's course. The author is grateful to Dr D. Baratoux, Dr. A. Suzuki, Dr. H. Sato, Dr. H. Ichikawa, Dr. J. Kimura and Dr. S. Ohtsuki for their important advice.

The author would like to thank all researchers in National Aeronautics and Space Administration (NASA) and European Space Agency (ESA) for their acquisition of scientific data and assistance in processing the data.

The author also wishes to thank Dr. S. Kameda, Mr. K. Yoshioka, Mr. G. Murakami, Mr. F. Ezawa, Mr. G. Ogawa, Mr. K. Kawaguchi, Mr. K. Hamada, Ms. A. Iwasaki, Mr. J. Kawaguchi, Mr. T. Koyama, Ms. M. Hirai, Mr. S. Kasahara, Mr. Y. Tanaka, Mr. J. Ono, Mr. K. Hikosaka, Mr. T. Kazama, Ms. A. Takamasa and other all colleagues in the University of Tokyo for their emotional assistance and friendship.

Finally, The author thanks his family for their financial support.

## References

- [1] J. Bandfield, P. Christensen, and M. Smith. Spectral data set factor analysis and end-member recovery- application to analysis of martian .... *J Geophys Res*, 105(E4):9573–9587, Jan 2000.
- [2] J. Bell, M. Wolff, P. James, R. Clancy, and S. Lee. Mars surface mineralogy from hubble space telescope imaging during 1994-1995: Observations, .... *J. Geophys. Res.*, Jan 1997.
- [3] J. BIBRING, Y. Langevin, F. Poulet, and A. Gendrin. Perennial water ice identified in the south polar cap of mars. *Nature*, 428:627–630, Jan 2004.
- [4] B. Cantor. Moc observations of the 2001 mars planet-encircling dust storm. *Icarus*, 186:60–96, Jan 2007.
- [5] B. A. Cantor, K. M. Kanak, and K. S. Edgett. Mars orbiter camera observations of martian dust devils and their tracks (september 1997 to january 2006) and evaluation of theoretical vortex models. *J. Geophys. Res.*, 111:E12002, Dec 2006.
- [6] P. Christensen, D. ANDERSON, S. CHASE, and R. Clark. Thermal emission spectrometer experiment: Mars observer mission. *J. Geophys. Res.*, 97(5):7719–7734, Jan 1992.
- [7] P. Christensen, J. Bandfield, and M. Smith. Identification of a basaltic component on the martian surface from thermal emission spectrometer .... *J Geophys Res*, 105(E4):9609 –9621, Apr 2000.
- [8] P. Christensen, B. Jakosky, H. Kieffer, and M. Malin. The thermal emission imaging system (themis) for the mars 2001 odyssey mission. *Space Sci Rev*, 110:85–130, Jan 2004.
- [9] P. Christensen, G. Mehall, S. Silverman, and S. Anwar. Miniature thermal emission spectrometer for the mars exploration rovers. *J. Geophys. Res.*, 108(E12):8064, Jan 2003.
- [10] P. Christensen and H. Moore. The martian surface layer. *Mars*, Jan 1992.
- [11] K. Edgett. Aeolian dunes as evidence for explosive volcanism in the tharsis region of mars. *Icarus*, 130:96–114, Jan 1997.
- [12] K. Edgett. Low-albedo surfaces and eolian sediment: Mars orbiter camera views of western arabia terra craters. *J. Geophys. Res.*, 107(E6):5038, Jan 2002.
- [13] C. Farmer, D. Davies, A. Holland, and D. Laporte. Mars-water vapor observations from the viking orbiters. *J Geophys Res*, 82:4225–4248, Jan 1977.
- [14] L. Fenton and M. Richardson. Martian surface winds: Insensitivity to orbital changes and implications for aeolian processes. *J. Geophys. Res.*, 106(E12):32885–32902, Jan 2001.

- [15] P. E. Geissler, J. R. Johnson, R. Sullivan, K. Herkenhoff, D. Mittlefehldt, R. Fergason, D. Ming, R. Morris, S. Squyres, L. Soderblom, and M. Golombek. First in situ investigation of a dark wind streak on mars. *J. Geophys. Res.*, 113:E12S31, Oct 2008.
- [16] R. Greeley. Martian variable features: New insight from the mars express orbiter and the mars exploration rover spirit. *J. Geophys. Res.*, 110:E06002, Jan 2005.
- [17] R. Greeley, R. Arvidson, P. Barlett, and D. Blaney. Gusev crater: Wind-related features and processes observed by the mars exploration rover spirit. *J. Geophys. Res.*, 111:E02S09, Jan 2006.
- [18] R. Greeley and J. D. Iversen. *Wind as a Geological Process: On Earth, Mars, Venus and Titan*, Jan 1987.
- [19] A. Jehl, P. Pinet, D. Baratoux, Y. Daydou, S. Chevrel, F. Heuripeau, N. Manaud, A. Cord, C. Rosemberg, and G. Neukum. Gusev photometric variability as seen from orbit by hrsc/mars-express. *Icarus*, 197(2):403–428, Oct 2008.
- [20] S. LEE, P. THOMAS, and J. VEVERKA. Wind streaks in tharsis and elysium - implications for sediment transport by slope winds. *J. Geophys. Res.*, 87(B12):25–41, Jan 1982.
- [21] S. W. Lee. Mars - wind streak production as related to obstacle type and size. *Icarus*, 58:339–357, Jun 1984.
- [22] M. C. Malin, J. F. Bell, B. A. Cantor, M. A. Caplinger, W. M. Calvin, R. T. Clancy, K. S. Edgett, L. Edwards, R. M. Haberle, P. B. James, S. W. Lee, M. A. Ravine, P. C. Thomas, and M. J. Wolff. Context camera investigation on board the mars reconnaissance orbiter. *J. Geophys. Res.*, 112:E05S04, May 2007.
- [23] T. Mccord and J. Westphal. Mars: Narrow-band photometry, from 0.3 to 2.5 microns, of surface regions during the 1969 . . . . *The Astrophysical Journal*, 168:141–153, Jan 1971.
- [24] A. S. Mcewen, E. M. Eliason, J. W. Bergstrom, N. T. Bridges, C. J. Hansen, W. A. Delamere, J. A. Grant, V. C. Gulick, K. E. Herkenhoff, L. Keszthelyi, R. L. Kirk, M. T. Mellon, S. W. Squyres, N. Thomas, and C. M. Weitz. Mars reconnaissance orbiter’s high resolution imaging science experiment (hirise). *J. Geophys. Res.*, 112:E05S02, May 2007.
- [25] M. Mellon. High-resolution thermal inertia mapping from the mars global surveyor thermal emission spectrometer. *Icarus*, 148:437–455, Dec 2000.
- [26] S. Memo. Meteorological results from the surface of mars: Viking 1 and 2. *J. Geophys. Res.*, 82(28):4559–4574, Jan 1977.

- [27] S. Murchie, R. Arvidson, P. Bedini, K. Beisser, J.-P. Bibring, J. Bishop, J. Boldt, P. Cavender, T. Choo, R. T. Clancy, E. H. Darlington, D. D. Marais, R. Espiritu, D. Fort, R. Green, E. Guinness, J. Hayes, C. Hash, K. Heffernan, J. Hemmler, G. Heyler, D. Humm, J. Hutcheson, N. Izenberg, R. Lee, J. Lees, D. Lohr, E. Malaret, T. Martin, J. A. MCGovern, P. Mcguire, R. Morris, J. Mustard, S. Pelkey, E. Rhodes, M. Robinson, T. Roush, E. Schaefer, G. Seagrave, F. Seelos, P. Silverglate, S. Slavney, M. Smith, W.-J. Shyong, K. Strohbehn, H. Taylor, P. Thompson, B. Tossman, M. Wirzburger, and M. Wolff. Compact reconnaissance imaging spectrometer for mars (crism) on mars reconnaissance orbiter (mro). *J. Geophys. Res.*, 112:E05S03, May 2007.
- [28] J. Mustard, S. ERARD, J. BIBRING, J. HEAD, and S. H. . . . The surface of syrtis major- composition of the volcanic substrate and mixing with altered dust and . . . *J Geophys Res*, 98(E2):3387–3400, Jan 1993.
- [29] S. Pelkey, B. Jakosky, and M. Mellon. Thermal inertia of crater-related wind streaks on mars. *J Geophys Res*, 106(E10):23909–23902, Jan 2001.
- [30] A. Peterfreund. Visual and infrared observations of wind streaks on mars. *Icarus*, 45:447–467, Jan 1981.
- [31] J. B. Plescia. Morphometric properties of martian volcanoes. *J. Geophys. Res.*, 109:E03003, Jan 2004.
- [32] N. Putzig, M. Mellon, K. Kretke, and R. Arvidson. Global thermal inertia and surface properties of mars from the mgs mapping mission. *Icarus*, 173:325–341, Feb 2005.
- [33] S. Ruff and P. Christensen. Bright and dark regions on mars: Particle size and mineralogical characteristics based on thermal . . . *J. Geophys. Res.*, 107(E12):5127, Jan 2002.
- [34] Sagan, J. Veverka, R. Steinbacher, L. Quam, and R. T. . . . Variable features on mars. iv. pavonis mons. *Icarus*, 22:24–47, Jan 1974.
- [35] R. Singer. Spectroscopic observation of mars. *Advances in Space Research*, 5:59–68, Jan 1985.
- [36] M. Smith, J. Pearl, B. Conrath, and P. Christensen. Mars global surveyor thermal emission spectrometer(tes) observations of dust opacity during . . . *J Geophys Res*, 105(E4):9539–9552, Jan 2000.
- [37] M. J. Strausberg. Observations of the initiation and evolution of the 2001 mars global dust storm. *J Geophys Res*, 110:E02006, Jan 2005.
- [38] P. Thomas. Mesoscale linear streaks on mars: environments of dust entrainment. *Icarus*, 162:242–258, Apr 2003.

- [39] P. Thomas, J. Veverka, D. Gineris, and L. Wong. “dust” streaks on mars. *Icarus*, 60:161–179, Jan 1984.
- [40] P. Thomas, J. Veverka, S. Lee, and A. Bloom. Classification of wind streaks on mars. *Icarus*, 45:124–153, Jan 1981.
- [41] T. Thorpe. The viking orbiter cameras’ potential for photometric measurement. *Icarus*, 27:229–239, Jan 1976.
- [42] J. Veverka, P. Gierasch, and P. Thomas. Wind streaks on mars: Meteorological control of occurrence and mode of formation. *Icarus*, 45:154–166, Jan 1981.
- [43] E. WELLS, J. VEVERKA, and P. THOMAS. Mars - experimental-study of albedo changes caused by dust fallout. *Icarus*, 58:331–338, Jan 1984.
- [44] S. Zhong. Migration of tharsis volcanism on mars caused by differential rotation of the lithosphere. *Nature Geosci*, Dec 2008.
- [45] M. ZUBER, D. SMITH, S. SOLOMON, D. MUHLEMAN, J. HEAD, J. GARVIN, J. ABSHIRE, and J. BUFTON. The mars-observer laser altimeter investigation. *J. Geophys. Res.*, 97(E5):7781–7797, Jan 1992.